Fiber Drawing: Beyond the scaling paradigm

by

Chong Hou

B.S. Physics, Peking University, 2009

Submitted to the Department of Materials Science and Engineering
in Partial Fulfillment of the Requirements for the Degree of

Doctor of Philosophy in Materials Science and Engineering

at the

MASSACHUSETTS INSTITUTE OF TECHNOLOGY

June 2016

Signature of Author..... Signature redacted .....
Department of Materials Science and Engineering
May 20, 2016

Certified by..... Signature redacted .....
Yoel Fink
Professor of Materials Science and Engineering
Professor of Electrical Engineering and Computer Science
Thesis Supervisor

Accepted by..... Signature redacted .....
Donald Sadoway
Chair, Departmental Committee on Graduate Students

Fiber Drawing: Beyond the scaling paradigm

by
Chong Hou

Submitted to the Department of Materials Science and Engineering
on May 12th, 2016, in Partial Fulfillment of the Requirements for the Degree of
Doctor of Philosophy in Materials Science and Engineering

ABSTRACT

The emergence of multimaterial fibers that combine a multiplicity of solid materials with disparate electrical, optical, and mechanical properties into a single fiber presents new opportunities for extending fiber applications. Different functional fiber devices have been fabricated with a thermal co-draw approach. In order to make the thermal co-draw feasible, only materials with similar viscosity at the draw temperature are used, which excludes a wide range of metal and semiconductors that have good electrical property but not compatible viscosity profile. From the fiber structure point of view, the nature of the fiber drawing process makes fabricating a large quantity of fiber with identical inner structures feasible. The scalability of thermal drawing approach offers access to large quantities of devices however constrains the devices to be translational symmetric. Lifting this symmetry to create discrete devices in fibers will increase the utility of fiber devices. Also, the surface of the fiber is rarely studied though complex inner structure have been fabricated for different functionalities. Functionalize the fiber surface would give fiber the ability to better interact with the outer environment.

This thesis seeks to address the abovementioned considerations, i.e. to expand materials selection for the fiber co-draw process and to explore variance of the fiber structure including breaking the inner structure translational symmetry and functionalize the outer surface. On the material side, a chemical reaction phenomenon is observed and studied in two different fiber drawing situations. In both cases, new composition is formed during the draw and play an important role in the formed fiber devices. On the structure side, relying on the principle of Plateau-Rayleigh instability, the fiber inner structure is designed to form a series of discrete semiconductor spheres contacting two metal buses after a thermal selective breakup process. This gives rise to photodecting devices in a silica-cladding fiber which shows a large working bandwidth. The fiber surface is also studied and successfully patterned with micron-scale features during the draw process. The formed patterned fiber surface shows potential in structural coloration and directional wetting.

Thesis Supervisor: Yoel Fink
Title: Professor of Materials Science and Engineering
Professor of Electrical Engineering and Computer Science

ACKNOWLEDGEMENTS

This thesis would not have been possible without the help, support, and friendship of many people. First and foremost, I would like to express my immense gratitude to my advisor Professor Yoel Fink. His vision and enthusiasm have inspired me to keep trying new things in my research. His profound knowledge and rigorous thinking have stimulated me to think deeper and wider. He has been an exceptional advisor throughout my time at MIT and will always be a mentor. I also would like to thank my thesis committee members, Professor John Joannopoulos and Professor Silvia Gradecak, for their availability, support, and guidance on my work.

This work could not have been accomplished without the dedicated work of my research group. I would like to thank Dr. Ofer Shapira and Dr. Nicholas Orf for introducing and training me the whole process of preform making and fiber drawing, thank Dr. Sasha Stolyarov and Dr. Sylvain Danto for teaching me how to make glass. I also benefited a lot from Sasha's help on scientific writing. I would like to thank Dr. Xiaoting Jia, Dr. Lei Wei for their generous help on a lot of experimental issues and I enjoy the fruitful discussion with them. I would also like to thank the remainder of the group for their assistance and support: Dr. Zheng Wang, Dr. Dana Shemuly, Dr. Fabien Sorin, Dr. Noemie Chocat, Dr. Alexander Gumennik, Dr. Guillaume Lestoquoy, Dr. Polina Pinkhasova, Dr. Tural Khudiyev, Dr. Jungtae Lee, Dr. Etgar Levy, Zachary Ruff, Benjamin Grena, Michael Rein, Jeff Clayton, Tara Sarathi, Rodger Yuan, and Gabriel Loke.

Many research technician at CMSE and ISN helps me a lot on the devices that I use for all the projects. I would like to thank Dr. Steve Kooi, Bill DiNatale at ISN, Tim McClure, Libby Shaw, Mike Tarkanian, Dr. Shiahn, Chen, Dr. Yong Zhang at CMSE for their patient training and support on the facilities. I would also like to thank Tina Gilman for helping me with a lot of issues outside research.

This period of time was joyful and pleasant thanks to many of my friends here in Cambridge and in China. I am thankful to all my family for being a constant source of support. Finally I am infinitely indebted to my parents, who have taught me the joy of learning and to whom I owe my presence at MIT.

Contents

List of Figures

Chapter I Introduction

1.1 Background

Fiber as a basic component in people's daily lives have been widely known and used for thousands of years. A recent archeological discovery indicates that over 30,000 years ago paleolithic hunter-gatherers used wild flax fibers to make cords, weave baskets, and sew garments[1]. Beginning from last century people begin to use fiber for optical applications such as transmitting signals in telecommunications, fiber lasers, etc[2–4]. And until recently in most cases, fiber exists as a single-material and serve simple functionality. In the last couple of years a new type of fiber emerges that composes a multiplicity of solid materials with disparate optical, electrical, and mechanical properties[5]. Different materials such as polymer, semiconductor and metals are selected to be integrated in one fiber and serve multiple functionalities. Fiber reflectors, thermal detectors, photodetectors, chemical sensors, surface-emitting fiber lasers, fiber diodes, and other functional fiber devices have been demonstrated with this approach[5–11].

General rule in fabrication of fiber

To fabricate this type of fiber, a group of materials with similar viscosity at the same temperature is selected to put inside a preform, either by inserting the material inside the cut pocket or by evaporating a thin film on top of another material. The preform shape could be rectangular or cylindrical, depending on the design of the fiber and normally

should take the main volume as the cladding is used for mechanically supporting the whole structure. The assembled preform is then sent to be consolidated in a hot furnace before going through the final thermal drawing. During the consolidation, the cladding polymer will get softer and begin to tangle with each other, hence making the whole preform one whole piece. Deformation is not expected in this process so a lower temperature than the drawing temperature is desired. But when temperature gets lower the time needed for the fully consolidation will be much longer. Exact temperature and time for the consolidation varies between different material, and different configuration. Figure I.1 illustrates some of the preform (polymer cladding, after drawing). Normally the indicator of a good consolidation is that the preform becomes transparent and the interface between layers disappears. Silica glass is different from polymer that it's not easy to get consolidated, so normally we use "pump and seal" method which details could be found in Chapter II.2.

During the draw process, 3 main parameters are considered i.e. the furnace temperature, the feeding speed and the drawing speed under the guidance of two main general rule. Firstly the drawing process preserve the volume. When the preform is heated up and becomes soft, the drawing speed is set to be hundreds of times faster than the feeding speed so when a short piece of preform is drawn into a long section, the cross section area correspondingly becomes much smaller. Specifically, we have the following equations:

$$\Delta V_p = \pi r_p^2 \Delta h_p = \pi r_p^2 v_p \Delta t = \Delta V_f = \pi r_f^2 \Delta h_f = \pi r_f^2 v_f \Delta t$$

$$\frac{r_p}{r_f} = \sqrt[2]{\frac{v_f}{v_p}} \qquad \text{Equation I-1}$$

The subscription p and f represents preform and fiber respectively. The symbol v is the speed of each part and the r represent the radius or the typical length of the cross section. The ratio between the radius of preform and the radius of fiber, normally called "draw down ratio", is the square root of the ratio between the fiber drawing speed and the preform feeding speed. For instance, with a 25mm diameter preform, feeding speed set at 0.5mm/min and drawing speed set at 5m/min, we could theoretically get a draw-down ratio of 100 and get fiber with 250 micron diameter. In practice, because the diameter change gradually it takes time for the whole process becomes equilibrated. The time it takes to become equilibrated relates to a lot of matters, e.g. the new material inside the preform that may change the heat distribution and change the mechanical strength of the preform, the temperature profile set by the 3-zone furnace, the change of drawing speed, etc.

The second general rule relates to the temperature setup. As shown in Figure I.1, different groups of materials have different viscosity profile. Chalcogenide glass (Se, As, S and their compound) have similar viscosity property as of thermalplastics that their viscosity decreases gradually as temperature rises, however the metal and metal alloy have a crystalline behavior that their viscosity keeps high and drops sharply at their melting point. A general rule regarding the temperature setup is that at this temperature all the material must flow, i.e. viscosity smaller than 10^6 $Pa*s$[12]. However it should also be avoided that all the materials' viscosity is too small. In that case the strength of the material is not enough to support the tension and the fiber would break. The ideal drawing temperature should be above the metal's melting point so that it can flow, and should also

keep the viscosity of the other materials especially the cladding polymer between 10^4 and 10^6 Pa*s in order to maintain the fiber structure.

Limitation and challenges

Over the years, a set of materials have been identified that fit these criteria and can be successfully co-drawn. High glass-transition temperature thermoplastics are used as the main supporting material (cladding) because of their variety, availability in bulk and film form, and excellent thermo-mechanical properties. Several thermoplastic polymers have been shown to be suitable for draw temperatures between 200 °C and 300 °C, including polyether sulfone (PES), polysulfone (PSU), polycarbonate (PC), cyclic olefin copolymers (COC), and polyetherimide (PEI). Correspondingly the chalcogenide glass is used to co-draw with these thermoplastics because of their similar viscosity at drawing temperature and their optoelectronic properties. And in order to get co-drawn with the polymer and the glass at around 200 °C, Tin based metal alloys are used because of their relatively low melting point.

As can be seen above, the material selection guided by the viscosity rule excludes a wide range of materials to be incorporated in the fiber. Many of these excluded materials exhibit superior optical and electrical properties but don't have the matched viscosity. For instance, many metal alloys have better conductivity than tin based alloys such as copper and silver, a bunch of compound semiconductor with different band gap would be used to tune the band gap structure such as GaAs, CdSe, ZnSe, etc, however their melting point or glass transition temperature are much higher than the drawing temperature suited for the

cladding thermalplastics. Although some CVD method could be used to add these materials into the hollow channel of the predrawn fiber[13], it lacks the control of materials' location and often has the problem of scalability.

Another obvious but easily omitted fact is that the structures designed inside fiber always maintain the translational symmetry. This translational symmetry roots from the continuous drawing process and guarantees the transportation of light and electrons along the fiber. Lifting this symmetry to create discrete devices in fibers will increase the utility of fiber devices. The surface of the fiber, on the other hand, is seldom studied though complex inner structure have been designed and fabricated for different functionalities. Functionalize the fiber surface would give fiber the ability to better interact with the outer environment, furthermore the synergy of both the inner device and outer surface would expand the functionality of the fiber devices.

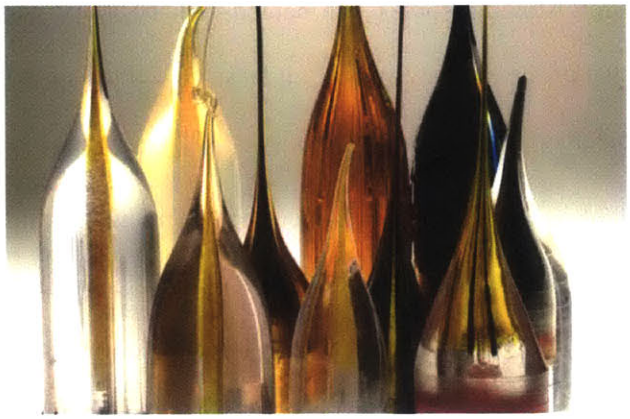

Supplementary Figure I-1 **Different polymer-cladding preform**

The top part of these preform illustrate the neck-down region characteristic in the thermal draw process. (Courtesy of Greg Hren)

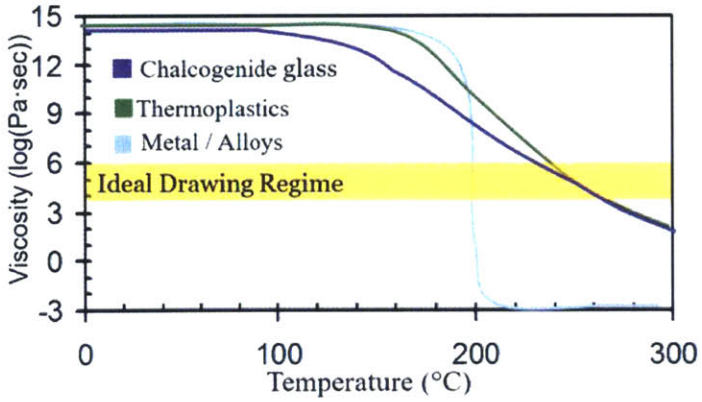

Figure I.1 **Different groups of materials' viscosity feature**

Amorphous material such as chalcogenide glass and thermoplastics have a gradually decreasing viscosity with rising temperature, while crystalline material such as metal and metal alloys keep the viscosity high until it reaches the melting point. At the melting point, the metal's viscosity drops sharply. The ideal drawing temperature should be above the metal's melting point so that it can flow, and should also keep the viscosity of the other materials especially the cladding polymer between 10^4 and 10^6 Pa*s in order to maintain the fiber structure.

1.2 Thesis Outline

This thesis seeks to address the abovementioned considerations, i.e. to expand materials selection for the fiber co-draw process and to explore variance of the fiber structure including breaking the inner structure translational symmetry and functionalize the outer surface. Two different projects are demonstrated for each purpose in Chapter 2 and Chapter 3.

Chapter 2 focuses on the material side and illustrates that a chemical reaction phenomenon is observed in two different fiber drawing situations. In both cases, new composition is formed during the draw and play an important role in the formed fiber devices. The chemical reaction happened during the thermal draw process not only brings in new composition to fiber structure which expands the materials selection widely, but also changed the view regarding the draw process. The thermal drawing process could be designed for chemical reaction since it naturally form a high temperature, high pressure condition.

Chapter 3 focuses on the structure side. Relying on the principle of Plateau-Rayleigh instability, the fiber inner structure is designed to form a series of discrete semiconductor spheres contacting two metal buses after a thermal selective breakup process. This gives rise to photodecting devices in a silica-cladding fiber which shows a large working bandwidth. The fiber surface is also studied and successfully patterned with micron-scale features during the draw process. The formed patterned fiber surface shows potential in structural coloration and directional wetting.

Chapter 4 concludes all the projects and predicts the future work regarding the materials selection expansion and structure variance on the fibers.

Chapter II Chemical Reaction in the Fiber Draw

2.1 ZnSe synthesized by *in situ* high-throughput reactive fiber drawing

Introduction

Preform-to-fiber drawing is a well-established process in as far as silica fibers are concerned[14–17], and has been applied recently to other glassy materials system with the drawing of in-fiber devices for applications ranging from medical to sensing.[5,8,18,19] In its conventional form, this process is characterized by heating a preform and continuously pulling it into a fiber, thereby reducing the cross sectional dimensions while maintaining the original materials and architecture assembled in the preform. While recent work has established that disparate materials could be combined in the process, this was still limited to the materials that flow at the draw temperature. The drawing of crystalline compounds is particularly challenging as they may undergo phase separation and decompose even if they can be drawn in their liquid state. To address these challenges recent work has explored the drawing process as a new nanocomposite synthesis tool whereby the preform reduction zone serves the role of a chemical reaction crucible, in which materials can physically mix, chemically react, and produce new compounds that precipitate directly into the fiber.[20–23] Recent examples include: 1) The addition of silicon carbide powder into silicon-core / silica-clad optical fibers for purifying the Si by gettering oxygen[21], 2) The production of silica fibers with cores comprised of the bismuth germinate family from the

reaction between bismuth oxides and germanium oxides[23], and 3) The synthesis of ZnSe from a chemical reaction at the interface between a $Se_{97}S_3$ film and a $Sn_{85}Zn_{15}$ electrode during fiber drawing[22]. Despite these proof-of-concept demonstrations, little has been done to optimize compound synthesis, comprehensively characterize the produced compounds, or study the underlying thermodynamics and kinetics driving the chemical reactions. In this work, we demonstrate a versatile and high-throughput method for synthesizing ZnSe during a fiber draw from a scalable multilayered structure comprised of elemental solid state Zn and $Se_{97}S_3$, and provide direct atomic-level compositional and structural analysis of the produced chemical compound. Furthermore, we experimentally probe the thermodynamics and kinetics of the in-fiber compound synthesis process. The methods described herein open a new path towards vastly expanding the set of possible materials and architectures compatible with multimaterial multifunctional fibers.

ZnSe is a widely used direct bandgap semiconductor with excellent optical and optoelectronic properties[24–29]. Recent efforts have focused on producing ZnSe structures in fibers with promising applications ranging from optical transmission to distributed photodetection[30,31]. Directly drawing ZnSe from a preform-confined melt to a fiber is complicated due to its high melting point of 1525 °C, high vapor pressure, and tendency to dissociate non-stoichiometrically[32,33]. Efforts to circumvent this problem have relied on post-draw chemical vapor deposition techniques[30,34]. Recently, it was discovered that ZnSe could be produced in situ during a fiber draw from the reaction of a Zn-containing electrode ($Sn_{85}Zn_{15}$) and a Se-containing thin film ($Se_{97}S_3$)[22]. There, the possibility of fabricating ZnSe over scalable lengths directly during fiber drawing was demonstrated, but the

methods used have two fundamental drawbacks. First, the location of the reaction was limited only to the surface of an electrode, while the bulk remained unutilized. Second, the electrode used was an alloy composed primary of another element (Sn), which had no contribution in the chemical reaction. Both significantly restrict the volume of ZnSe that can be produced and complicate characterization efforts. Here, we demonstrate a new method to synthesize ZnSe which addresses the above shortcomings. This method, based on thermal deposition of multiple alternating layers of nanoscale-thick elemental Zn and $Se_{97}S_3$, significantly increases the volume of ZnSe produced and importantly, enables unambiguous materials characterization.

Fabrication method and characterization

Figure II.1 (a-b) depicts the details of the preform assembly and periodic multilayer architecture of the two chemical precursors necessary to form ZnSe. The multilayer Zn/$Se_{97}S_3$ structure is evaporated onto a wide conductive polycarbonate (CPC) pad which is contacted by a metal ($Sn_{63}Pb_{37}$) bus. Evaporated on the opposite side of the Zn/$Se_{97}S_3$ multilayers is a 50 μm thick, 10 mm wide $Se_{97}S_3$ film which bridges the multilayer structure to another $Sn_{63}Pb_{37}$ metal bus, forming a two-terminal circuit. The preform cladding material is polysulfone (PSU), which co-draws well with $Se_{97}S_3$, CPC, and $Sn_{63}Pb_{37}$ at ~ 260 °C.[35]

$Se_{97}S_3$ was synthesized from high-purity elements (Alfa Asear) using the standard melt quenching technique[22]. Zn powder for evaporation is 99.99% from Alfa Asear. $Sn_{63}Pb_{37}$ alloy ribbons are from Indium Corporation. Polysulfone (PSU) and Conductive

Polycarbonate (CPC) are from Patriot Plastics. $Se_{97}S_3$ is evaporated on top of a 75 μm thick PSU sheet. $Se_{97}S_3$ and Zn are alternatively evaporated on top of a 0.254 mm thick CPC sheet. Evaporation is conducted on a Ladder Research evaporator. A preform is fabricated by cutting pockets in 4.75 mm thick PSU slabs, placing the corresponding material in PSU, and consolidating under pressure of 200 psi at 195 °C for one hour and then cooling down to room temperature. The fiber is drawn down from the 20 mm x 9 mm x 200 mm preform in a furnace with a middle-zone (around preform cone) temperature of 260-270 °C. The fiber size varies with the ratio of the drawing speed to the feed speed and is controlled to be between 0.4 mm and 2 mm (short side length).

During the draw, the Zn and Se-rich layers mix, react, and precipitate ZnSe. Although the melting temperature of elemental Zn (420 °C)[33] exceeds the preform drawing temperature, the 50 nm thick Zn layers do not impede the draw and completely react with the Se. The wide $Se_{97}S_3$ layer and synthesized ZnSe form a heterojunction in this two-terminal circuit as will be discussed later in the text. The use of the CPC electrode allows enlarging the effective junction area while kinetically mitigating capillary breakup that would otherwise occur from the sheer flow at a liquid-metal/Se interface during the draw. The relatively low resistivity of CPC (102 - 106 Ω * cm) also facilitates charge transport from the thin film formed on one side of the CPC pad to the metal bus on the other side.[19] The assembled structure is thermally consolidated under a pressure of 200 psi at 195 °C to form a monolithic preform, which is drawn into meters of fiber as shown in Figure II.1 (c-e).

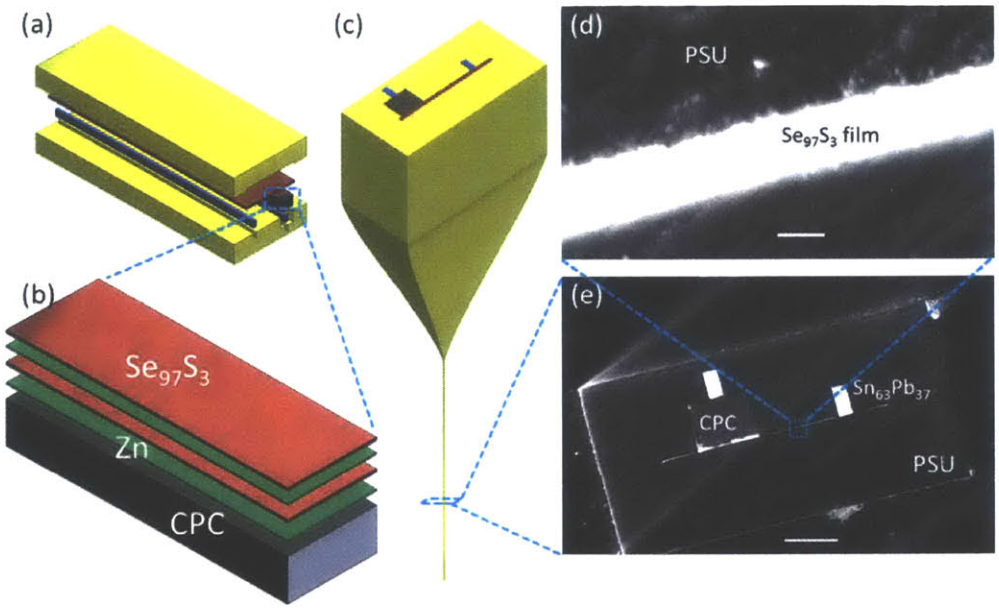

Figure II.1 **Preform and fiber fabrication process**

(a) Schematics of the preform assembly showing the PSU cladding (yellow), CPC electrode (black), $Sn_{63}Pb_{37}$ electrodes (blue), and the $Se_{97}S_3$ film (red). (b) Zoomed-in illustration of the alternately layered $Se_{97}S_3$ (red) and Zn (green) films, which are thermally evaporated onto the CPC slab (black). Eleven layers of $Se_{97}S_3$ (1 μm each) and ten layers of Zn (50 nm each) are evaporated in total, while the figure shows only a part of them. (c) Illustration of the thermal drawing process. (d), (e) Scanning electron microscope (SEM) images of the fiber cross section. Scale bars: (d) 1 μm, (e) 200 μm.

Post draw, atomic-level inspection at the surface of CPC where the Zn and Se97S3 mixed is performed using a high-resolution transmission electron microscope (HRTEM). Figure II.2 (a) is a micrograph of the cross section of the as-drawn fiber which shows a clear crystallized area surrounded by amorphous material. Figure II.2 (b) illustrates the fast Fourier transform (FFT) image of the marked crystalline region in Figure II.2 (a), which indicates that the image is viewed along the <011> zone axis of the zincblende structure, as corroborated by comparison with the simulated diffraction pattern as shown in Figure

II.2 (c). The two parallel lines highlighted in Figure II.2 (a) represent {111} planes. The spacing between the neighboring planes is 0.328 nm, from which the lattice constant of the material is calculated to be 5.68 Å. The fast Fourier transform (FFT) image of the marked crystalline area in Figure II.2 (b) indicates that the image is viewed along the <011> zone axis of the zincblende structure, as compared with Figure II.2 (c) the simulated diffraction result of (011) plane in the zincblende structure. A direct measurement on the crystalline area reveals that the distances between two consecutive lines are 0.3293 nm (3.293 nm/10) and 0.327 nm (4.58 nm/14) along two directions respectively, as shown in Sup. Fig. II-1 (a), (b). According to Sup. Fig. II-1 (c), the lattice constant can be calculated as

$$a = \frac{0.328\text{nm}}{\frac{1}{\sqrt{3}}} = 0.568\,nm$$

The slight difference between the distances in different directions could be caused by measurement error, or imperfectness of lattice structure. From information of Figure II.2 (a-c) and Sup. Fig. II-1, we can infer the material composition. Firstly it cannot be elemental material, because neither S, Se, nor Zn has a crystal structure that corresponds to the diffraction pattern shown in Figure II.2 (b). Specifically, crystallized S has an orthorhombic structure and Se is trigonal, and Zn has a hexagonal lattice structure and lattice constant of 4.95 Å(c_0) and 2.67 Å(a_0).[36] For possible compounds, zinc sulfide (ZnS) has a zincblende structure with a lattice constant of 5.41 Å[37,38] which is much smaller than the calculated value. However, ZnSe matches the structure and lattice constant with a reference value of 5.67 Å.[37] According to the above fact and the lattice structure we measure, we can infer that the material we observe is crystalline ZnSe.

An energy-dispersive X-ray spectroscopy (EDX) mapping using scanning transmission electron microscopy (STEM) as shown in Figure II.2 (d) identifies the elements present in the same area as marked in Figure II.2 (a). This elemental distribution map shows that Zn and Se dominate in the crystalline area and that they mix uniformly at the nanoscale as shown in Figure II.2 (d), which further supports the claim that the ZnSe compound is synthesized during the fiber draw. A point-by-point scan with TEM and EDX on different sections along the fiber axis reveals that the ZnSe islands exist randomly near the surface of CPC surrounded by Se-S. Considering all the Zn is used up in reaction with Se-S (as discussed later), the formed compound volume can be estimated to be ~1% of total $Se_{97}S_3$. With more layers of alternating structure, the volume percentage can be further increased.

In addition to HRTEM, we also characterize the fiber using Raman spectroscopy. The Raman spectra of the thin film illustrated in Figure II.3 show that two distinctly different peak patterns exist at different regions along its length. In the region away from the CPC electrode where no ZnSe is expected, labeled A, all of the Raman spectra have a strong peak at 238 cm^{-1}. This is completely consistent with the Raman response of trigonal Se, which has a single strong peak at ~ 237 cm^{-1} corresponding to the A1 mode.[39,40] This is expected since the film in this region of the fiber is pure $Se_{97}S_3$. In the region directly beneath the CPC electrode where the ZnSe synthesis is expected to occur, labeled B, a different Raman distribution is measured at certain (but not all) locations. A weak peak shows up at 252 cm^{-1}. This is also completely consistent with the Raman spectra of thin film ZnSe where there is essentially only one peak at 251 cm^{-1}, which corresponds to the 1LO band of ZnSe.[30,41,42] The difference in signal strength between Se and ZnSe arises

from the intrinsically strong response from Se and the fact that the amount of ZnSe is much smaller than Se.

The spot size of the laser used in the Raman measurement is 1 μm, which is about the thickness of the $Se_{97}S_3$ thin film in fiber. The ZnSe/Se junction area has a much smaller thickness of about 50 nm determined by the thickness of Zn layers. Because the location of the laser beam is hard to control precisely, the laser beam could fall on the following positions (Sup. Fig. II-2): in region A, independent of slight offsets in beam alignment, most of the beam area would cover $Se_{97}S_3$ film, as shown on position 1. In region B, depending on the alignment, the laser beam could cover mostly $Se_{97}S_3$, as position 2 and 3, or mostly overlap the CPC, as in position 4. For scenarios similar to position 1, 2, and 3, the Raman peak of Se present at 238 cm^{-1} would be measured. For beam positions close similar to position 4, because part of the laser beam covers ZnSe and little covers $Se_{97}S_3$, the Raman signal at those positions will mainly reflect the existence of ZnSe, but the intensity will not be strong (as witnessed in the data of Figure II.3 (red trace)). Also at those positions, the peak representing Se is so weak that it could not be measured above the background noise. Comparison between these two patterns further confirms compound formation.

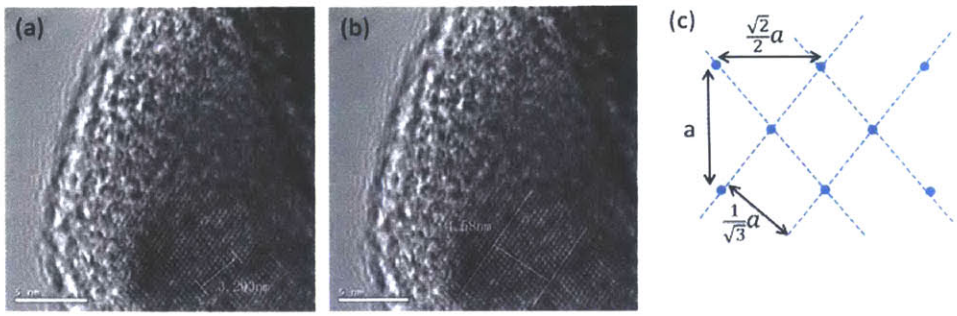

Supplementary Figure II-1 **TEM Measurement on ZnSe crystalline area**

(a), (b) Measurement between parallel lines in two directions. (c) The lattice alignment when viewed in {110} direction for fcc lattice (zinc blende belongs to fcc).

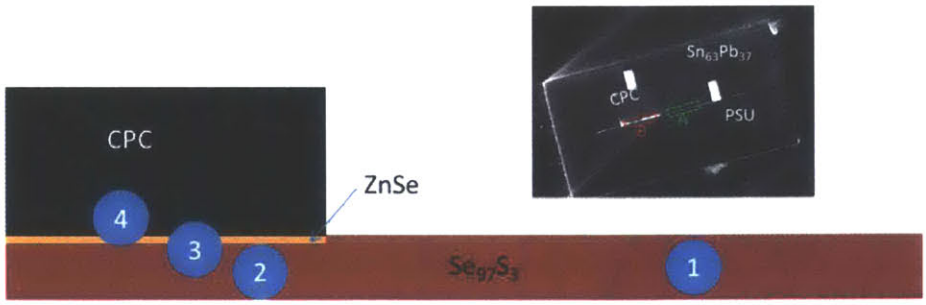

Supplementary Figure II-2 **Schematic representation of Raman laser spot position**

The blue circles denote the laser spot. In region A, laser beam easily overlaps with the $Se_{97}S_3$ film (position1); in region B, only a spot at position 4 would register a ZnSe Raman peak, while the laser spot in positions such as 2 and 3 would mostly register a peak from Se. Inset: SEM image of fiber cross section.

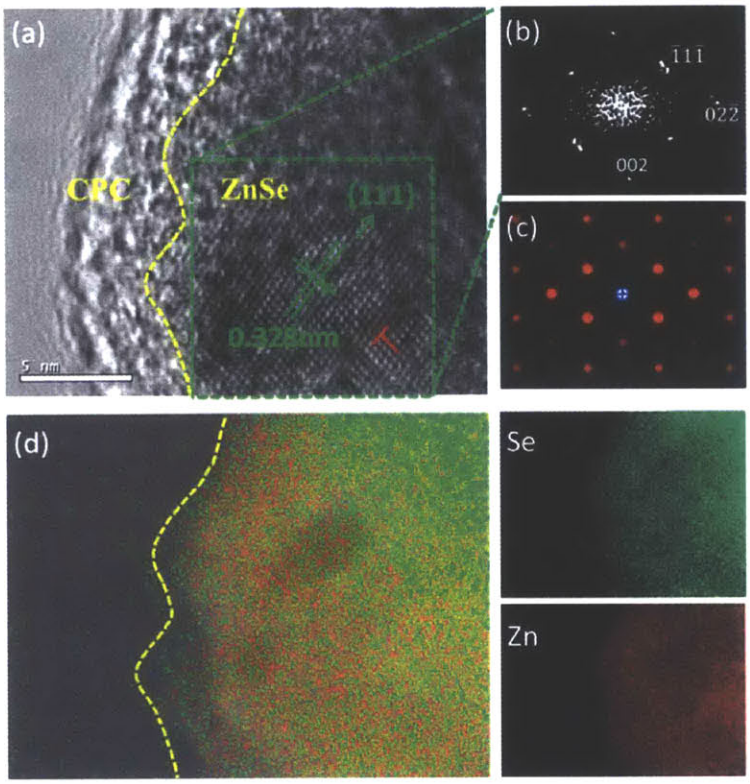

Figure II.2 **TEM characterization of crystallized area in amorphous surrounding**

(a) A high magnification TEM micrograph of crystalline ZnSe surrounded by amorphous material. The red 'T' indicates an edge dislocation. The dashed yellow curve obtained from (d) indicates the boundary between CPC and ZnSe. Scale bar: 5 nm. (b) Fast Fourier transform (FFT) image of the area marked by a dashed green square in (a). (c) Simulated diffraction pattern along the [011] direction of ZnSe with zincblende structure. (d) Energy-dispersive X-ray spectroscopy (EDX) mapping of the same area in (a). Green dots represent distribution of Se, and red dots represent distribution of Zn. The dashed yellow line is the same as in (a).

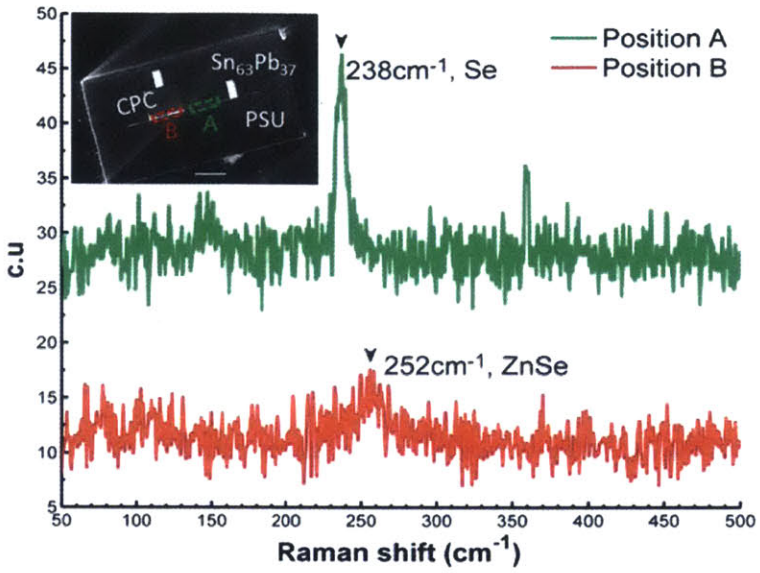

Figure II.3 **Raman characterization**

Laser wavelength = 532.17 nm, beam radius = 500 nm. The red trace and green trace correspond to Raman spectra recorded from two different regions, as illustrated in the inset. Label A and B correspond to the regions that contain only $Se_{97}S_3$ and that contain $Se_{97}S_3$ with ZnSe, respectively. Inset scale bar: 200 μm.

Discussion

We proceed to discuss the mechanism by which this unique synthesis method can occur during fiber drawing. Noticing that Zn has a melting temperature of 419 °C (therefore, it is still solid at the draw temperature) and ZnSe melts at 1525 °C, it is surprising that a solid-state compound is synthesized from a solid-state precursor material in such a short time (the dwell time of the preform cone in the furnace is ~ 20 minutes). In order to investigate how this happens, thermogravimetric analysis (TGA) and differential scanning calorimetry (DSC) are carried out on a sample comprised of alternatingly evaporated

$Se_{97}S_3$/Zn layers. The thickness of the layers is the same as that in the preform, thereby mimicking the above-described structure in the preform. The heating process for both tests simulates the same fiber drawing conditions. Specifically, the material is first heated to around 270 °C, dwells for approximately 10 minutes, and then gets cooled down to room temperature.

During the TGA measurements, materials with a low melting temperature and high vapor pressure will be easily vaporized and those with lower vapor pressures will remain. FigureII.S3 shows the TGA results on the alternatingly evaporated Zn/$Se_{97}S_3$ sample. The blue line showing the change of sample weight indicates that $Se_{97}S_3$ begins to evaporate at ~200 °C. The red line shows the rate of change of the sample weight. (Note that the dip in the red line and the sudden increase in weight at ~240 °C is an artifact of transient glitch in the software.)

The sample used for TGA has the same thickness of materials as those used in preform. During TGA, Zn reacts with some of the $Se_{97}S_3$ and forms ZnSe compound, and the rest of $Se_{97}S_3$ is gasified and then blown away during TGA, only leaving the compound in the sample holder. This process leads to the weight loss in Sup. Fig. II-3 and optical change in the inset of Figure II.4 (a). While in preform-to-fiber fabrication, the optical change in the thin film is not obvious due to two reasons: 1, the compound is formed on the surface of black CPC; 2, most $Se_{97}S_3$ is preserved inside fiber during drawing process. The color of CPC and $Se_{97}S_3$ dominates that of ZnSe, thus the optical change of the thin film in the fiber is not easily observed.

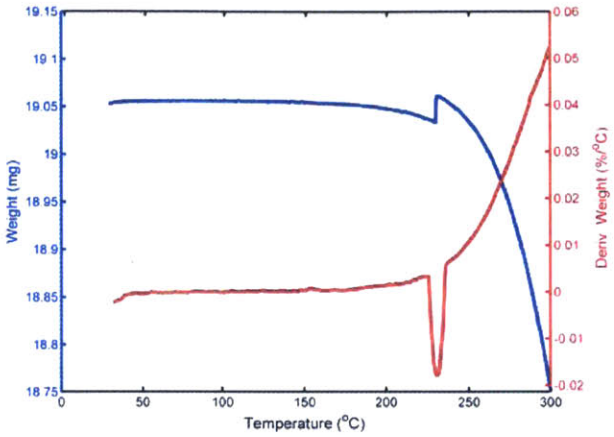

Supplementary Figure II-3 **Thermogravimetric Analysis Plot**

The blue line shows the sample weight changes along with temperature and the red line shows the change rate of the weight. The dip in the red line and the sudden increase in weight at ~240 °C is an artifact of transient glitch in the software.

The inset of Figure II.4 (a) shows the sample before and after the TGA measurement. Before the measurement, the Zn/ $Se_{97}S_3$ sample has a dark metallic color. After the measurement, however, the material remaining in the container appears dark yellow and is identified to be polycrystalline ZnSe by X-ray Diffraction (XRD) as shown in Figure II.4 (a), indicating that a chemical reaction occurred during the measurement. The XRD measurement also reveals that ZnSe has a grain size of around 63 nm. Because of the limited crystalline size, the XRD pattern of the sample shows broadening. From the information of XRD peak location (θ) and the corresponding peak width (B) we can retrieve the information about crystallite size using Williamson-Hall method[43]:

$$B \cdot \cos(\theta) = \frac{k\lambda}{D} + \eta \cdot \sin(\theta) \qquad \text{Equation II-1}$$

B and θ are the width and the position of the peak, respectively, D is crystallite size, λ is the radiation wavelength, k is a constant (=1 in our case), and η is the microstrain.

Sup. Fig. II-4 shows the Williamson-Hall Plot corresponding to XRD analysis in Figure II.4 (a). Every dot in this plot represents the peak showing up in the XRD pattern. As indicated by the formula II.S1, we plot $B\cos(\theta)$ vs $\sin(\theta)$, and then the slope gives out microstrain value (η) and the intercept reveal the information of crystalline size (D).

From the plot we can see the formed ZnSe has a crystallite size of 63 nm, which is approximately the same as the thickness of Zn layer. This grain size is the same order as the thickness of each Zn layer in the preform. Based on this observation, we propose the mechanism that is illustrated in Figure II.4 (b), where the Zn layers are deformed and broken into small pieces as they flow and react with the surrounding Se fluid, precipitating out ZnSe particles. The break-up of the Zn layer is caused by the stress generated during drawing process, which is further determined by the local temperature and drawing speed. The nanometer-scale Zn thin films help achieve a thorough chemical reaction, as indicated by XRD result in Figure II.4 (a).

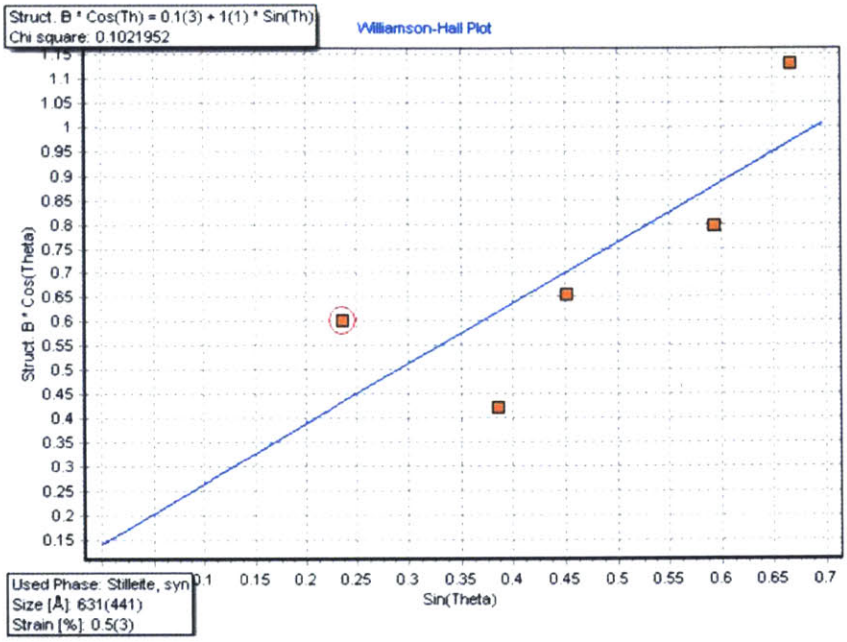

Supplementary Figure II-4 **XRD analysis for crystalline size**

The regression line between the cosine and sine of theta reflects the crystallite size as well as the strain.

DSC measurements provide independent and direct evidence of a chemical reaction between Se and Zn as they are heated. As seen from Figure II.4 (c), in the first DSC run, two peaks show up, where the first and second peak correspond to the crystallization and melting of Se, respectively. Importantly, after the crystallization peak, the heat flow remains negative (except the melting peak of Se) despite the fact that the sample is being heated. This release of heat can only be explained by the initiation of an exothermic chemical reaction between the constituent materials, which is shown in Equation II-2[44] and schematically in Figure II.4 (d).

$Zn+Se=ZnSe, \Delta H=-163 kJ/mol$ Equation II-2

After the material is cooled, a second DSC run is performed on the same sample. During this second run the heat flow is always positive, which means no chemical reaction is taking place. This indicates that the synthesized compound has not decomposed and that all the Zn has been used up in the chemical reaction during the first DSC run.

The newly created compound can act as a functional component in fiber devices. Since ZnSe is a direct bandgap semiconductor with a bandgap of 2.7 eV[37] (corresponding to 459 nm), it is an attractive material for optoelectronic devices in the visible wavelength range. The fiber's optoelectronic properties are detailed in Figure II.5. Prior to optoelectronic characterization, the fiber is annealed at 150 °C for 1 hour in order to crystallize the wide $Se_{97}S_3$ layer. In the crystallized state, the conductivity of $Se_{97}S_3$ improves by about 8 orders of magnitude[35,45] as depicted in Figure II.5 (a). The current-voltage characteristics both in the dark and under illumination for the annealed sample are shown in Figure II.5 (b). The $Sn_{63}Pb_{37}$ electrode directly contacting $Se_{97}S_3$ is forward biased. The diode-like electronic behavior in the dark suggests the existence of a built-in potential in the circuit. In contrast, a control fiber without any Zn shows a purely ohmic response, as determined from the linear I-V curve depicted in Figure II.5 (c).

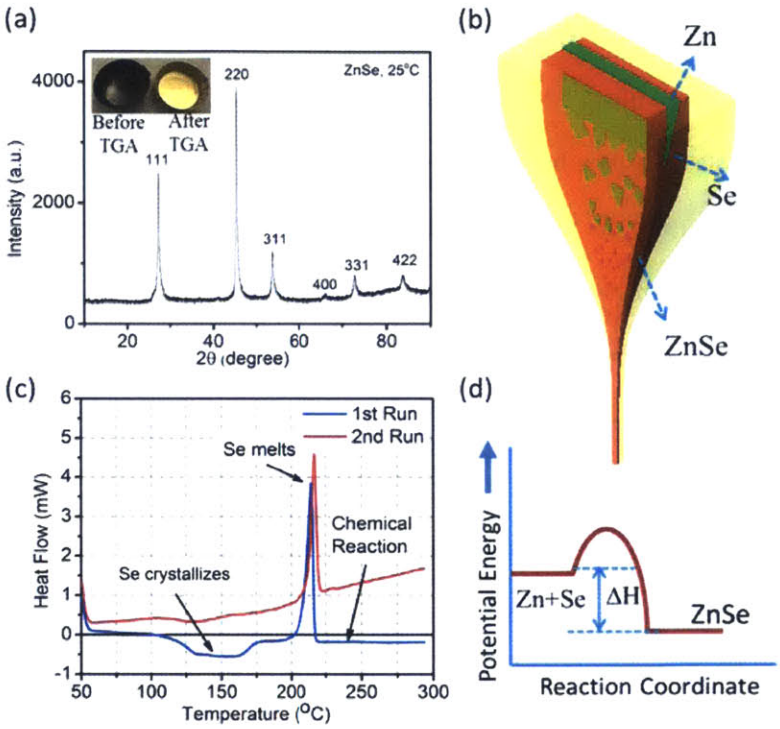

Figure II.4 **Thermal analysis of chemical reaction**

(a) X-ray Diffraction (XRD) spectrum shows that the synthesized ZnSe from the TGA test is mostly polycrystalline. Inset: image of ZnSe after TGA (right) compared with evaporated $Se_{97}S_3$ with Zn (left). (b) Schematic diagram depicting the proposed mechanism of the fiber-draw-induced chemical reaction. The Zn layer breaks up and reacts with the surrounding Se to form ZnSe compound. (c) DSC test runs twice: first run shows the process of Se crystallization and melting. The negative heat flow after the crystallization of Se indicates that an exothermic chemical reaction is taking place. However, in second run only the Se melting peak shows up and heat flow is constantly positive. (d) The reaction diagram shows the exothermic nature of this reaction.

From the structure of the two-terminal circuit, the built-in potential could potentially result from several interfaces, including (1) $Sn_{63}Pb_{37}$ and CPC, (2) CPC and ZnSe, (3) ZnSe and $Se_{97}S_3$, and (4) $Se_{97}S_3$ and $Sn_{63}Pb_{37}$. In order to determine which interface results in the rectifying junction, another fiber with a similar structure is drawn,

annealed, and tested for comparison. This fiber also has a layer of $Se_{97}S_3$ connected to $Sn_{63}Pb_{37}$ and CPC, but Zn is entirely omitted from the structure. Electrical measurements show that this fiber has a linear I-V curve, as plotted in Figure II.5 (c), which indicates that ohmic contact is established on both ends of $Se_{97}S_3$ thin film as well as between CPC and $Sn_{63}Pb_{37}$. This result rules out the possibility of situation (1) and (4). On the other hand, CPC is polycarbonate immersed with carbon powder and electrically behaves metallically. The work function of carbon is known to be approximately 4.8 eV.[46] ZnSe is known as a semiconductor with band gap of 2.7 eV and work function of 4.84 eV.[37,47] $Se_{97}S_3$ has a 1.9 eV band gap and a 4.2 eV electron affinity.[48] Based on the above information, a band diagram is proposed to explain the observed fiber electrical behavior as shown in Figure II.5 (d). Because of the difference between their Fermi energy, when in contact, both $Se_{97}S_3$ and ZnSe bend their bands to form a heterojunction at their interface. From the figure we can see that the electrons are forbidden to transport through the interface of ZnSe and $Se_{97}S_3$; however, holes can easily drift from ZnSe to $Se_{97}S_3$ with the help of the built-in electric field. A built-in potential of 0.31 eV is calculated based on the above reference values. Given the Fermi level and bandgap of both materials, the contact between ZnSe and CPC can be ohmic or Schottky depending on whether the majority carrier in ZnSe are holes or electrons.[49] Since there is no doping in ZnSe and undoped ZnSe is known to be p-type[50], the contact between ZnSe and CPC should be ohmic, thus ruling out situation (2). Therefore, we can deduce that the rectifying junction can only be formed at the interface between ZnSe and Se.

The proposed band diagram for this device is shown in Figure II.5 (d). Here, we can see that electrons are forbidden to transport through the interface of ZnSe and $Se_{97}S_3$; however, holes can easily drift from ZnSe to $Se_{97}S_3$ with the help of the built-in electric field. A built-in potential of 0.31 eV is calculated based on the referenced values[22,37,46,47], as shown in Figure II.5 (d).

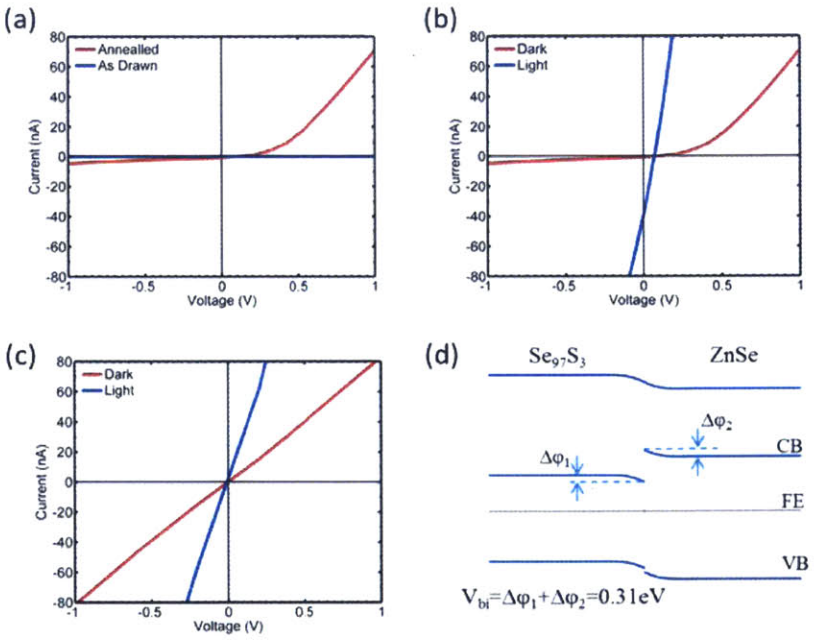

Figure II.5 **Optoelectronic characterization and Band Diagram**

(a) Comparison between as-drawn fiber and fiber after annealing under dark. (b) Electrical behavior in dark and under illumination for $Se_{97}S_3$ thin film embedded with ZnSe particles indicates a rectifying junction exists in the circuit, (c) Linear I-V property of pure $Se_{97}S_3$ shows the presence of an ohmic contact between $Se_{97}S_3$ and CPC, $Sn_{63}Pb_{37}$. (d) Band diagram shows that a rectifying junction is formed between $Se_{97}S_3$ and ZnSe, CB: conduction band, FE: Fermi energy, VB: valence band, V_{bi}: built-in potential.

In conclusion, we demonstrate a layer-by-layer method to synthesize ZnSe in situ during fiber drawing and provide direct atomic-level observation and analysis of the synthesized compound. The alternating evaporation approach central to this fabrication process significantly increases product throughput and enables precise control over the reaction location inside the fiber. The methods described herein set the stage for expanding the materials and architectures possible with fiber drawing, thus paving the way towards more complex and sophisticated fiber devices.

Devices and methods

TEM image and STEM-mode EDX mapping is taken on JEOL 2010F, with an accelerating voltage of 200 kV. The TEM sample is prepared using Leica EM UC6 microtome. The fiber is first trimmed at the surface and then cut into a <50 nm thick flake. Then the flake is transferred to a TEM 300 square mesh copper grid (the grid is covered with a Carbon film). SEM images are taken on JEOL 6060, with an accelerating voltage of 4 kV. Fiber sample is first put in epoxy. After epoxy cures, epoxy with fiber surface is polished mechanically with a roughness down to 0.3 μm. The confocal Raman spectroscopy is performed with a Horiba HR800 in backscatter geometry. A 532 nm laser is used as the excitation source and is focused onto the sample with a 100X NA0.9 objective. XRD is taken on PAnalytical_X'pert Powder X-ray diffractometer. Thermogravimetric Analysis was done on TA Instruments TGA Q50, and Differential Scanning Calorimetry was performed on PerkinElmer Instruments Pyris Diamond DSC in a nitrogen atmosphere. Electrical measurements for as-drawn samples and annealed samples are taken with a

Hewlett Packard 4284a meter. The fiber sample is illuminated by Electrix Illumination E428 with a power of 20 Watts. The fiber annealing process is done at 150 °C under vacuum for 1 hour.

2.2 Crystalline Silicon Core Fibers from Aluminium Core Preforms

Introduction

Silicon (Si) and its oxide silica (SiO_2) have both played an important role in modern day electronics and communications[51–60]. In recent years the opportunities for tighter integration between electronics and photonics have led to the emergence of the field of Si photonics where wafer processes are used to combine the best features of both materials[61–64]. In a mirror effort the advanced demonstrations of incorporating Si into Fibers have been explored in electronics and photonics, such as photodetection[13], Fiber battery[65], Fiber solar cell[66,67], electro-optical modulation[68], material engineering[69], non-linear optics[70,71], and pressurized Si sphere fabrication[72], etc. Two disparate methods of producing Si-core silica-cladded Fibers have been reported, the first relies on the physical flow process and the second on a chemical reaction internal to a pre-fabricated Fiber. In the first method, high purity Si is placed inside a silica preform and drawn down into a silica Fiber with a molten Si core[72,73]. The second involves the use of high pressure Si precursor gas (SiH_4) to deposit Si inside a pre-fabricated hollow channel Fiber via a chemical vapor deposition (CVD) process[74]. The CVD method is more versatile while the thermal drawing approach is more scalable.

The placement of disparate materials thermally drawn into close proximity at elevated temperatures presents compelling opportunities for inducing chemical reactions between the constituent materials[75–77] that could in principle provide the versatility of

chemical reactions with the scalability of Fiber drawing. Results of this approach which we call Fiber-draw synthesis (FDS) to date have been confined to reactions in only small domains at an interface between materials.

In this work, we utilize the redox reaction between aluminium (Al) and silica (SiO_2) during Fiber drawing to produce a Fiber with a different core composition than that of the preform. This occurs through the following reaction:

$$4Al + 3SiO_2 \rightarrow 2Al_2O_3 + 3Si$$

At high drawing temperature the metallic Al reacts with the cladding material SiO_2 and reduces the Si. The products (Al_2O_3 and Si) then get phase separated thus forming a pure Si-core in silica Fiber. The reaction, diffusion and the phase separation all take place at an elevated temperature close to the Fiber draw temperature.

Fiber fabrication and characterization

The proposed method centers on a technique so-called preform-to-Fiber fabrication by thermally drawing a macroscopic solid-state preform into extended lengths of uniform Fibers, as shown in Figure II.6 (a). The preform consists of one piece of Al wire (3 cm long, 250 μm diameter) placed inside a silica tube (inner diameter 300 μm, outer diameter 600 μm). This assembly is further cladded with two concentric silica tubes (one with 1 mm inner diameter, 6 mm outer diameter, and the other one with 6 mm inner diameter and 12 mm outer diameter), as shown in Fig II.6 (b). The chamber where the Al wire resides is then pumped to 10^{-3} mbar and sealed with silica rods on both ends to prevent Al in contact with air. The preform with the Al core is then heated up to 2200 °C in Argon atmosphere

and pulled into meters-long Fibers with the diameters of around 500 μm. During the Fiber draw, Al melts and reacts with the surrounding silica cladding, and reduce Si atoms out of silica [78]. Si atoms accumulate during this process and finally occupy the entire core, resulting in a Si-core Fiber with silica cladding, as shown in Figuger II.6 (c).

Figure II.7 (a) shows an optical image of the Fiber and indicates a change in core material as the Fiber is drawn. From top to bottom, the color of the Fiber core is seen to transit from light yellow to black. Scanning electron microscope (SEM) and energy-dispersive X-ray spectroscopy (EDX) analyses are taken at four locations along the length of the Fiber. Figs. 2b-e are SEM images of the cross sections at locations 1-4 marked in Figure II.7 (a), respectively. Comparing these four figures, one notice there are light-grey dots appear within the core region in Figure II.7 (c-e). The grey dot in Figure II.7 (c) is so small that is hardly noticed, but can be seen more clearly from EDX mapping on a zoomed-in area as shown in Figure II.7 (o). The dots in Figure II.7 (d) and Figure II.7 (e) are much larger. It is worth mentioning though that these dots in Figure II.7 (c-e), however, are quite different in forming mechanism and in 3D shape. In Figure II.7 (c) the dot is actually a precipitated spherical drop composed of a majority of Si. But in Figure II.7 (e) the dot is actually cross section of the long crystalline Si wire. To explain the difference, we take samples from two locations along the Fiber for comparison. One sample, corresponding to the top panel of Figure II.8, is taken in the core region of the Fiber approximately at location #2 in Figure II.7 (a). Sup. Fig. II-6 (a) shows the TEM image of the sample. It is clear from the image that this sample contains several dots with similar sizes. These dots are about 100 nm diameter, and are all surrounded by a circle. From Figure II.8 (d) we know that the

circle is Al-rich and the center of the dot is Si-rich. Considering that this TEM image is actually side view of the Fiber, we could conclude that the dots at location #2 shown in Figure II.7 (c) are spheres in the Fiber core. Another sample, corresponding to the bottom panel of Figure II.8, is taken at the core-cladding interface of the Fiber near location #4 in Figure II.7 (a). In this sample, other than the Pt part, the rest is divided into two parts by an interface. Further analysis reveals that one part is amorphous and the other part is crystalline (see Figure II.8 (g)). In Sup. Fig. II-6 (b) the interface is through the whole sample, indicating that the core is long axially. Considering the continuous black core in the Fiber we conclude that the dot in Figure II.7 (e) is the cross section of a long Si wire. The yellow dashed squares in Sup. Fig. II-6 (a) and Sup. Fig. II-6 (b) mark the location where the TEM images in Figure II.8 (a) and Figure II.8 (g) are taken. The insets of the figures illustrate the sample position at the Fiber cross section (Blue denotes the core, and the red line denotes the sample position).

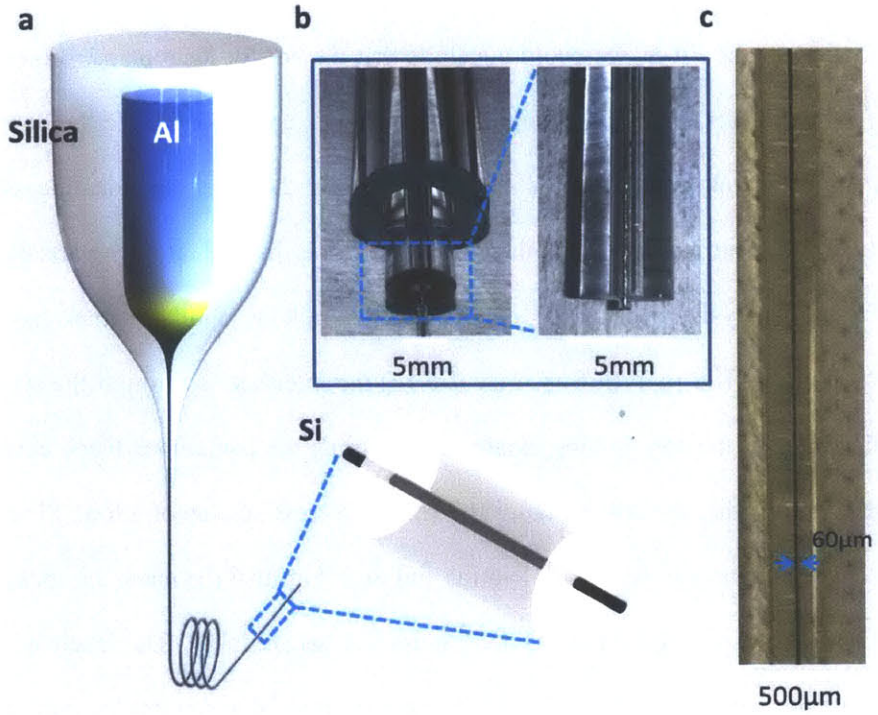

Figure II.6 **Aluminium-core-silica-cladding preform drawn into silicon-core Fiber**

a, the schematic diagram of the drawing process. A piece of Al wire is placed in the core of a preform and drawn with silica cladding. But what eventually comes out instead is a Si-core Fiber. **b,** the optical image of the preform before the shiny Al core is sealed in the cladding. **c,** the optical image of the drawn Fiber with a black Si core. The core diameter is about 60 μm.

The EDX analyses around these areas are shown to the right of the four SEM images and confirm that the dots in locations #3 and #4 are composed of high-purity Si. In Figure II.7 (f-q), green, red, and yellow colors denote element Al, Oxygen (O), and Si, respectively. In Figure II.7 (f, j, n) (location #1), the core is composed mainly of Al and O. In Figure II.7 (g, k, o) (location #2), a small agglomeration of Si appears while Al and O

still dominate the core area. In Figure II.7 (h, l, p) (location #3), a large Si core is formed in the center of the core area, surrounded by a thick layer composed of Al and O. Finally, in Figure II.7 (i, m, q) (location #4 which is in the black core section), Si occupies the entire core region, leaving Al to only a thin layer between the core and the cladding.

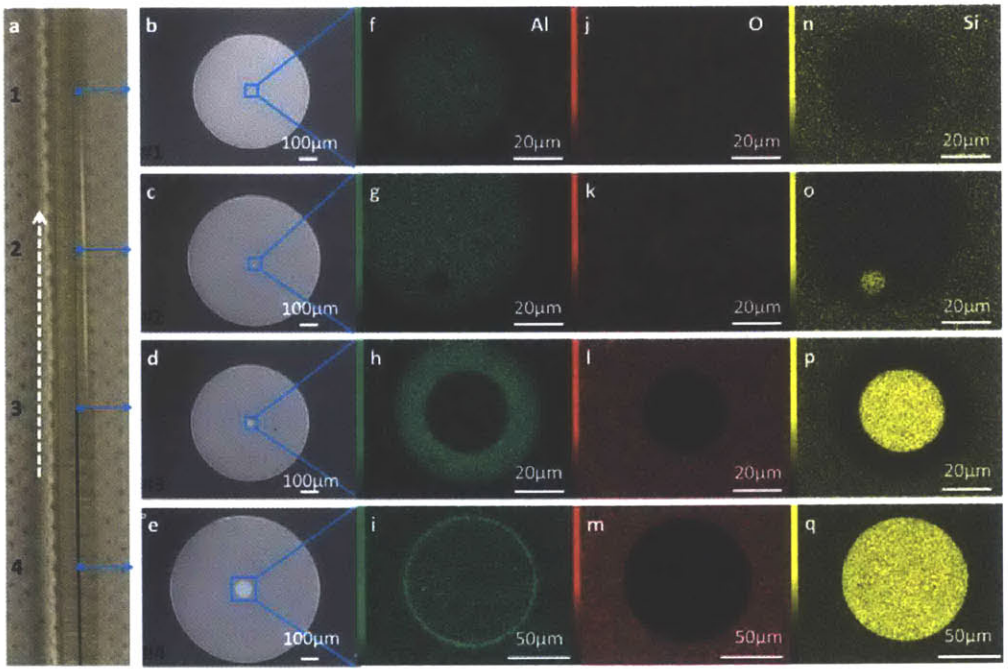

Figure II.7 **Transition of Fiber core**

a, the optical image of a piece of Fiber where a light-yellow core transits to a black core. The white dashed arrow illustrates the Fiber drawing direction. **b-e,** the SEM images of the cross sections at the 4 labeled locations in **a**. **f-q,** the EDX mappings of the marked area in **b-e** correspondingly. Green, red, and yellow denote element aluminium (Al), oxygen (O), and silicon (Si), respectively.

To further explore the differences between the light-yellow and black core regions, transmission electron microscopy (TEM) based analyses are performed at two different

cross-sections (see Sup. Fig. II-5 for preparation of TEM samples), corresponding approximately to locations #2 and #4, respectively.

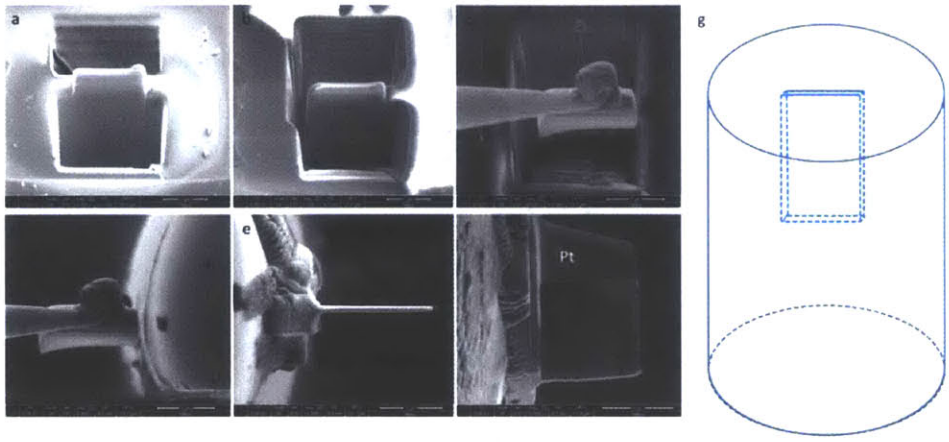

Supplementary Figure II-5 **Preparation of TEM samples on silica-clad fiber**

a, Use ion beam to etch materials on two sides of the sample. **b,** Ion beam cuts one edge. **c,** attach sample to the tip and use the ion beam to cut the other edge. **d,** attach the sample to the TEM grid. **e,** view of the sample from the top. **f**, view of the sample from the side, the top part is deposited Pt, and the bottom part is the sample. The sample showing here is taken from the core-cladding interface of the Fiber close to location #4. **g,** sketch of the sample inside the Fiber.

In the core of a yellow-core region we find that spherical drops form scattered along the axial direction (Sup. Fig. II-6). If we focus on one of these spherical drops we obtain the results shown in the top panel of Figure II.8. Figure II.8 (a) shows that the sphere is about 100 nm in diameter and is surrounded by a circle of different materials. The diffraction pattern in Figure II.8 (b) shows that the materials are mostly amorphous, and the EDX maps in Figure II.8 (c-e) reveal that the sphere is Si rich while the surrounding halo is Al rich. A line scan result across the sphere, as shown in Figure II.8 (f), confirms this observation. In the case of the black core region (bottom panel) we find distinct

properties across the core-cladding interface. As shown in Figure II.8 (g), the dashed yellow line separates a crystalline part from an amorphous part. Figure II.8 (h) is the diffraction pattern taken on the crystalline side and indicates that the material is crystalline with a diamond cubic structure as viewed along <111> zone axis. The two parallel lines highlighted in Figure II.8 (g) represent {110} faces. The distance between the neighboring faces is 0.192 nm, from which the lattice constant of the crystalline material is calculated to be 0.543 nm. This detailed lattice structure information helps identify that the crystalline material is Si: On one hand, crystalline Si has a diamond cubic structure.[79] On the other hand, viewing it from <111> zone axis one could get the following 2-D structure as shown in Sup. Fig. II-7. Each dot in the figure represents a series of atoms along the <111> axis at that position. So the distance between two parallel planes in Figure II.8 (g) is represented by OH in Sup. Fig. II-7. Suppose the lattice constant of Si is a, the distance between the two parallel planes in Figure II.8 (g), i.e. OH in Sup. Fig. II-7, is equal to $\sqrt{2}a/4$. According to the measurement, that distance is 0.192 nm, so the lattice constant is calculated to be 0.543 nm, which is exactly the lattice constant of Si.[79]

In addition to TEM analysis, XRD and Raman microspectroscopy are also performed to identify the Si core and study its crystallinity. A piece of Si wire (~3 cm long) is taken from the Fiber by etching off the cladding. The XRD data is taken on the Si wire in a Rigaku SmartLab X-ray diffraction system. As shown in Sup. Fig. II-8, the 3 peaks which correspond to Si (111), (220), (311) indicate that the Si wire is polycrystalline with cubic crystalline structure and in the Fd-3m space group (PDF card 00-027-1402). Raman spectrum is taken under illustration of 633 nm laser on the cross section of the Si-core Fiber

and on the surface of a single crystalline Si wafer. As shown in Sup. Fig. II-9, the Si-core Raman spectrum has a peak at 521.0 cm^{-1} with a 4.1 cm^{-1} full width at half maximum (FWHM) while the single-crystalline Si has a Raman peak at 519.9 cm^{-1} with a FWHM of 5.8 cm^{-1}. This similarity further supports the crystallinity of Si core in the Fiber. The difference, albeit small, may result from structural imperfections and residual stresses arising from the thermal expansion mismatch between the Si core and the silica clad.[73] X-ray diffraction (XRD) and Raman spectrum[80,81] help identify that the Si core wire is polycrystalline, which is similar to that of the core drawn from molten-core method[67,73] (Sup. Fig. II-8, II.S9). The EDX mappings shown in Figure II.8 (i-k) clearly demonstrate that the thickness of the Al-rich layer surrounding the Si core is about 100 nm. Finally, the line scan in Figure II.8 (l) demonstrates the purity of Si in the core region.

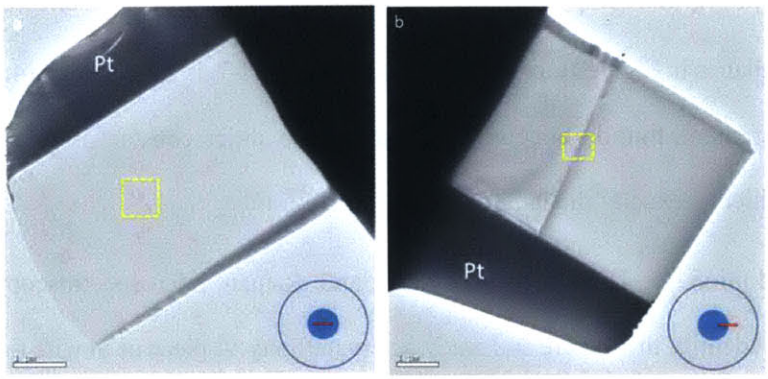

Supplementary Figure II-6 **TEM images of samples from different locations**

a, the sample is from core region of Fiber near location #2. **b,** the sample is from core-cladding interface of Fiber near location #4. For both figures, the yellow dashed square denotes the position of the TEM images in Fig. 3(a, g), and the red bar in the inset of each figure illustrates the corresponding sample position in the Fiber (the blue-filled round represents the core and the circle represents the clad). In **a**, the sample is taken from the center of the core. In **b**, the sample is taken from the interface between the core and the clad.

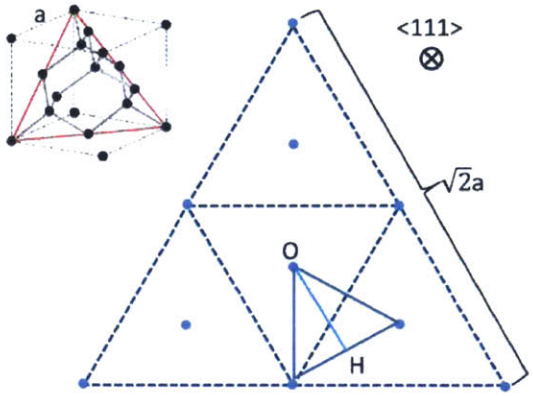

Supplementary Figure II-7 **Illustration of crystalline Si in <111> axis**

Each blue dot represents a series of Si atoms when viewed in <111> direction. OH is the distance between the two parallel planes. The inset is the crystalline structure of Si.

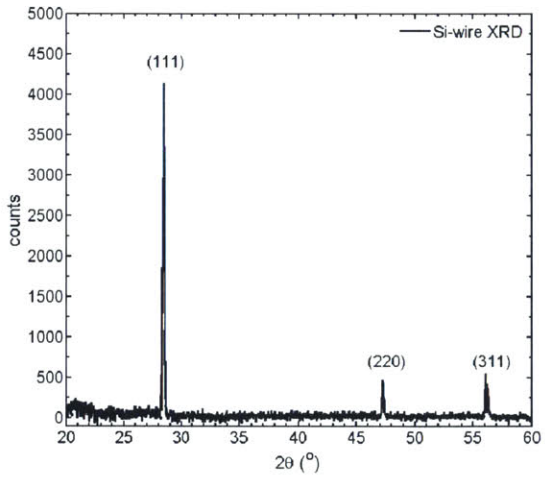

Supplementary Figure II-8 **Si wire XRD result**

The XRD pattern shows that the Si wire is polycrystalline.

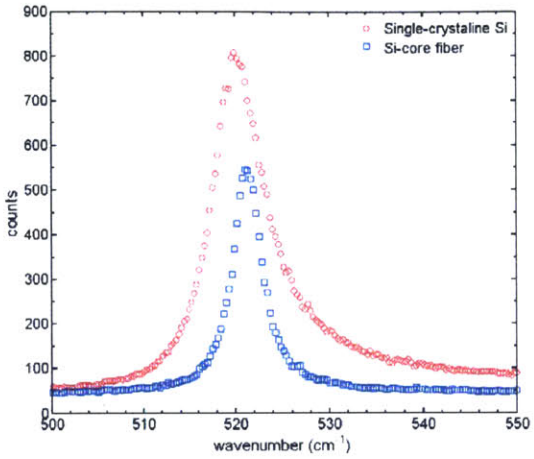

Supplementary Figure II-9 **Raman spectrum comparison**

The red circles are taken from a single-crystal Si wafer and the blue squares are taken from the Si core of the Fiber.

Incorporation of crystalline Si into Fibers can enable Fiber optoelectronic applications. Current approaches include the molten core drawing (MCD) or High pressure chemical vapor deposition (HPCVD) with post-annealing process, leading to the demonstration of in-Fiber semiconductor devices[13,66,72,80]. Here we characterize the electric performance of the Si core fabricated by the FDS method. A piece of Si wire is taken from the Fiber by etching off cladding with 40% hydrofluoric acid. As shown in Figure II.9 (a), 20 nm thick Al and 150 nm thick gold (Au) are deposited on selected locations of a piece of Si wire. Because the diameter of the Si wire is so much larger than the thickness of the deposited metals (100 μm vs 170 nm), Si wire is actually not connected to the electrodes shown in Figure II.9 (a), instead the situation is shown in Sup. Fig. II-10. To solve this problem, on one hand, the silver paint is applied to the two end electrodes to make sure the

wire is connected to the electrodes on two ends, on the other hand, the probes for voltage measurement directly contact the top of the wire to make sure the probes are connected to the Si wire through the Au/Al layer.

During the measurement, the 4-point probe method is used to prevent the possible Shottky junction between the Si wire and the electrodes. The current is supplied through two end electrodes, and the voltage is measured across two neighbor electrodes (i.e. 1-2, 2-3, 3-4) in between of the two end electrodes. The I-V curve corresponding to different electrodes pair is shown in Sup. Fig. II-11, and further processed to Figure II.9 (b). From Figure II.9 (b), one could get the resistance per unit distance on the Si wire. Because the Si wire is measured to be 100 μm in diameter, the resistivity is calculated to be 0.3 Ω cm (conductivity 3.4 S cm^{-1}), which is about the same order as that of the annealed Si core from the HPCVD method and several orders of magnitude smaller than that of intrinsic Si[53,80]. Though exact dopant concentration is not obtained through the resistivity value alone, it is highly possible that the Si core is doped instead of intrinsic. Considering the composition of the initial core, one can infer that the dopant material is aluminum. Given the measured resistivity as well as the dopant information, we can extrapolate that the dopant concentration is about 10^{17} cm^{-3}.[82] The dopant concentration is probably related to the solubility limit of Al in Si at a lower temperature. Further optimization of structure and fabrication process is supposed to achieve better control of material qualities.

The Si wire with all the cladding etched off is also observed under AFM, as shown in Sup. Fig. II-12. The image is taken after the AFM data is processed so that the surface

is flattened. The surface of the Si wire is measured to have an Rq of 1.04 nm on a 2 μm by 2 μm area. This indicates that the Si wire has a fairly smooth surface.

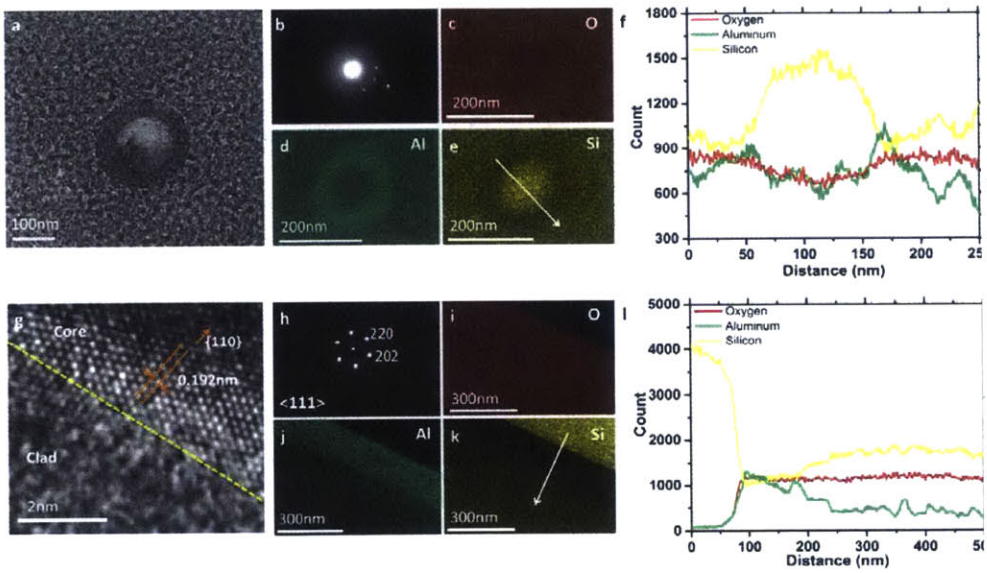

Figure II.8 **Nano-scale analyses on Fiber core**

On the top panel, **a-f** data are measured inside the core region of the Fiber with a yellow core (near location #2 in Figure II.7 (a)). **a**, TEM image, the dot is one of the many dots seen on the sample. **b**, the diffraction pattern indicates that the sample is mostly amorphous. **c-e,** EDX mappings on **a**, red, green, and yellow denote O, Al, and Si, respectively. **f**, EDX line scan result. The white arrow in **e** shows the line scanning path corresponding to **f**. On the bottom panel, **g-l** data are measured at the core-cladding interface of the Fiber with a black core (near location #4 in Figure II.7 (a)). In **g**, the yellow dashed line indicates the interface between the crystalline part (core) and the amorphous part (clad). The parallel orange lines are {110} faces, and the distance between them is measured 0.192nm. **h** is taken from crystalline side of the yellow line, and the zone axis has been tilted to <111>. **i-k,** EDX mappings on **g**, red, green, and yellow denote O, Al, and Si, respectively. **l**, EDX line scan result. The white arrow in **k** shows the line scanning path corresponding to **l**.

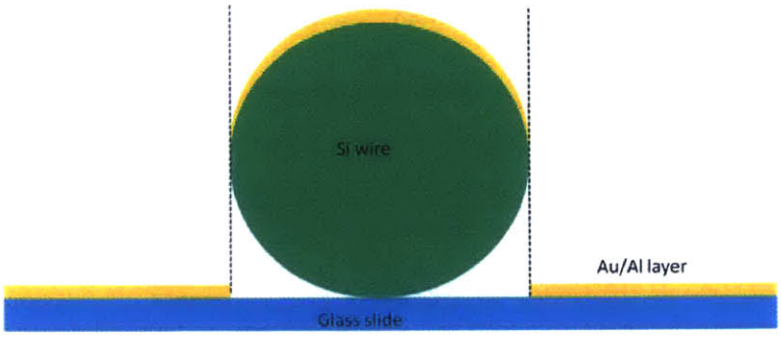

Supplementary Figure II-10 **Illustration of deposition of Al/Au on top of Si wire**

This figures show that the Si wire is so large that the deposited Au/Al layer on top of Si wire could not be connected to the Au/Al layer on top of the glass slide.

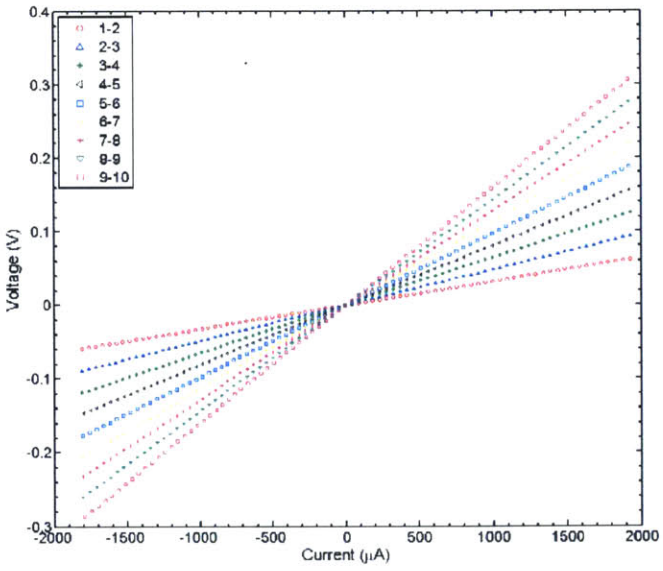

Supplementary Figure II-11 **I-V curve for different voltage electrode pairs**

As the distance between different electrodes varies, the resistance (the slope) changes proportionally.

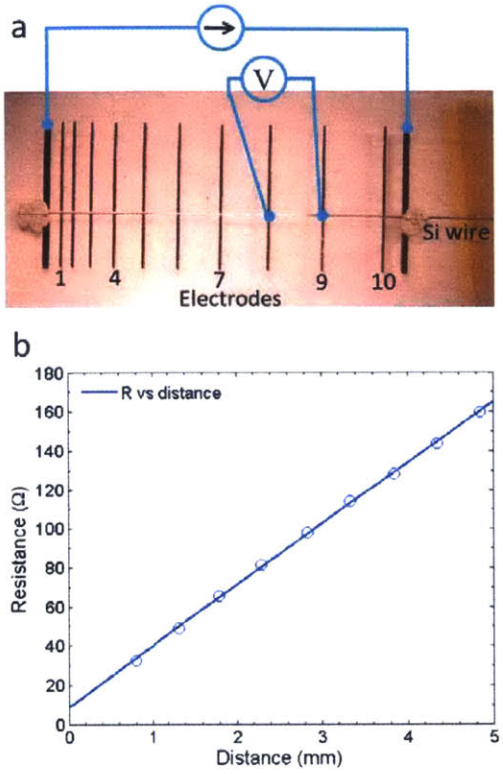

Figure II.9 **Si wire electrical characterization**

a, the 4-point probe measurement set up. A piece of Si wire (~3 cm long) is taken from Fiber by etching off the cladding, and then 20 nm Al and 150 nm Au are deposited on selected locations (2 outmost electrodes for current source and 10 electrodes for voltage meter contact marked 1 to 10). During the measurement, the probe directly contacts the Al/Au layer on top of Si wire. Current is provided from electrodes from two ends and voltage is measured across neighborhood electrodes in between of the two end electrodes. **b,** The resistance across neighbor electrodes are calculated from **a** and are plotted against their corresponding distance. Linear regression on the points gives information of Si resistivity.

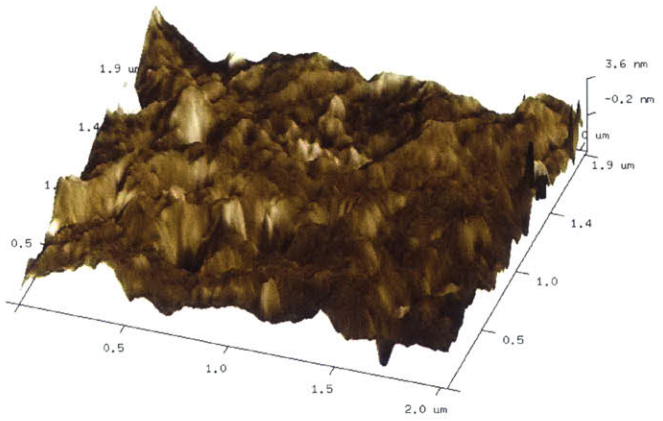

Supplementary Figure II-12 **AFM of Si core surface (flattened)**

This image is taken at the top of the Si wire and flattened. The surface variance is <5nm in a 2 micron by 2micon area, indicating that the surface is smooth.

Si-core forming mechanism

The mechanism for Si material to appear in the Fiber is a chemical reaction between the Al core and silica cladding. Al has a melting temperature of 660.32 °C so it melts when fed into the heating zone and keeps its molten state until oxidized[83]. Also as an active reducer, Al reduces the surrounding silica and produces Si atoms and Al_2O_3 molecules[84]. The drawing temperature of 2200 °C is higher than alumina's melting point so that alumina cannot form a shield to protect Al atoms from oxidizing as it would at room temperature. Without the protection of alumina, the reaction between Al atoms and silica happens fast due to two factors: (1) as described by Arrhenius's law, reaction rate relates to temperature exponentially. When the temperature increases by about 2000 K, the reaction rate is orders

of magnitude higher. (2) The largely increased diffusivity at high temperature helps transfer products away from the reaction site at the interface, thus effectively decreasing the products' local concentration and maintaining the chemical reaction. Figure II.10 (a) is a schematic depicting how the chemical reaction happens at the core-cladding interface.

In addition, although the reduced Si atoms are mixed with the other product Al_2O_3 and not-yet-reacted Al atoms in the beginning, their solubility properties play an important role in separating them and finally forming a Si core. Most importantly, Si is completely miscible with Al in the liquid state, but their solubility with Al_2O_3 is comparatively low[83,85]. As more and more Al_2O_3 is produced, the excessive Al_2O_3 precipitates out of molten Al. Meanwhile, Si stays with molten Al because of their miscibility. Since the density of molten Al and Si are about 2.4 g cm^{-3} and are smaller than that of molten alumina which is about 2.8 g cm^{-3} [85–87], molten Al-Si floats up and molten alumina sinks to the bottom as shown in Figure II.10 (b). As the draw and chemical reaction progress, more and more Al in the Al-Si melt gets consumed hence much less Al_2O_3 remains in the melt, while Si keeps accumulating in the Al-Si melt on top of alumina melt. Finally when Al is completely consumed in the reaction, a highly pure Si melt is obtained on the top of the core. Further drawing results in a highly pure Si-core Fiber. Figure II.10 (c-e) depicts the above-mentioned core composition change during the draw.

Solubility not only plays an important role in obtaining a Si-core Fiber, but also explains the embedded spheres seen in Figure II.8 (a) as well. Those Si-rich spheres in alumina are from the small amount of Si which dissolves in molten alumina in the heating

zone. As the Fiber is pulled out of the furnace and the temperature drops, the solubility of Si in Al_2O_3 decreases. The excess Si then precipitates out and forms spheres in alumina.

Besides accumulating with the help of miscibility properties, the Si core is also purified by going through the furnace. Because the preform is fed into the furnace from the top side and the Fiber is pulled out of the furnace from the bottom, the difference between the hot furnace temperature and room temperature constructs a temperature profile in which Si melts when entering the hot zone and solidifies when leaving the hot zone. This temperature profile provides the zone melting condition to further purify the Si core[88]. Additionally, Si is crystallized when it cools down from liquid state after pulling out of furnace[89].

Discussion

Our method remains further optimization for future applications. For example, the size of Si-core could be significantly reduced by redesigning the core-clad ratio and adjusting the Fiber draw parameters. Redraw technique could also be applied to achieve nanometer-scale Si wires[72]. Also the thin interface layer that lies between the core and the cladding as seen in Figure II.7 (i) and Figure II.8 (j) could be of interest for the potential advantage on oxygen gettering and surface modification for the post-drawing process[67,90]. The smoothness of the Si is verified in the atomic force scan (AFM) image (Sup. Fig. II-12, Supplementary Note 3). Last but not least, The mechanism of producing Si during Fiber drawing is also applicable to other reductive metals, e.g. Titanium (Ti) or Calcium (Ca), which could reduce Si because of their more negative reduction potentials[91].

To conclude, we demonstrate a new way to fabricate a high-quality crystalline Si-core Fiber by thermally drawing a preform consisting of low-cost metal. The methods described herein set the stage for extending the materials and architectures selections with Fiber drawing, thus paving the way towards more sophisticated Fiber-based devices.

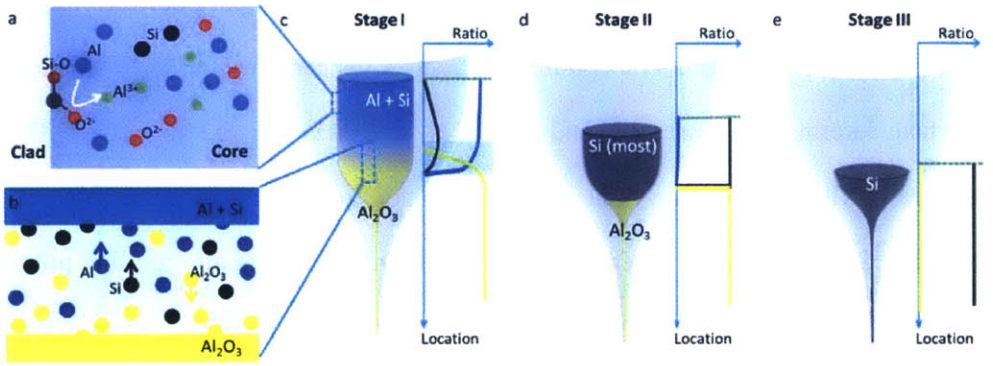

Figure II.10 **Si-core forming mechanism in Fiber draw**

a, the chemical reaction at the core-cladding interface. Al atoms (blue) break Si-O bond, reduce Si (black), release O^{2-} ions (red), and change to Al^{3+} ions (green). All the products of ions and atoms dissolve in the Al melt and diffuse into the core. **b,** the Si atoms (black), because of their miscibility, diffuse and remain in the Al melt (blue), while ions of O and Al form Al_2O_3 molecules (yellow) and precipitate out at the bottom. **c-e,** sketches of the situations of the core in the heating zone throughout the drawing process. As the draw continues, more and more Si atoms accumulate in the Al-Si melt and eventually one obtain a highly pure Si melt on top of the Al_2O_3 with all the Al consumed in the redox reaction (Stage II). Further drawing then results in a highly pure Si-core Fiber (Stage III). The diagrams corresponding to ech figures demonstrate the ratio of different materials along the core axially. Blue, black and yellow denote Al, Si, and Al_2O_3, respectively. The green dashed line which gets lower and lower during the draw marks the position of the core. The cyan shadows in **b** and **c** illustrate the location of the transition region.

Devices and methods

For the preform preparation we use the fused-quartz tubes and rods supplied by Technical Glass Products and the Al wire from Alfa Aesar. The fused-quartz capillary Fiber (300 μm inner diameter and 600 μm outer diameter) is from Molex Incorporated (product # TSP300794). The coating material on the capillary Fiber is burned with flame and cleaned up with isopropanol.

The 0.25 mm diameter Al wire is first inserted into the capillary Fiber and then put into a fused-quartz tube with an inner diameter of 1 mm and outer diameter of 6 mm (1x6 tube). Two 1 mm diameter fused-quartz rod are also inserted into the 1x6 tube, one on top of the capillary Fiber and the other in the bottom of the capillary Fiber. The whole assembly is put into a fused-quartz tube with an inner diameter of 6 mm and outer diameter of 12 mm. With the help of propane flame, one end of the structure is fused and the whole assembly is pumped to vacuum and the other end is fused under vacuum.

The Fiber drawing process starts at the temperature of 2150 °C and the drawing process continues at 2200 °C. The preform is fed into the furnace from top with a speed of 1mm min^{-1}, and the Fiber is pulled out from the bottom end of the furnace with a speed of 660 mm min^{-1}. The Fiber is further coated with coating material which is called "DSM Desotech 3471-3-14(941-314) Desolite single coat coating" and cured by an in-line ultraviolet coating system.

The SEM images and related EDX mappings on cross sections of the Fibers are taken with the JEOL 6010LA SEM. The TEM samples are prepared in the Helios Nanolab 600 Dual Beam Focused Ion Beam (FIB) Milling System. Ion beams are firstly used to

etch away the materials on two sides of the defined region on the Fiber cross section, and the leftover piece of material is taken out and attached to the TEM grid. Then this piece of sample is further thinned with ion beam (the top Platinum (Pt) is deposited to secure and protect the sample). The whole process is shown in Sup. Fig. II-5 (a-f), and Sup. Fig. II-5 (g) illustrates the sample taken from the Fiber. From Sup. Fig. II-5 (f) and Sup. Fig. II-5 (g) we know that the TEM image shows the situation of the side-section of the Fiber.

The TEM images and related EDX scans are taken using the JEOL 2010 FEG Analytical Electron Microscope. The Raman spectrum is taken in the Horiba Jobin Yvon LabRAM Model HR800. The XRD spectrum is taken in Rigaku SmartLab with a parallel-beam optics and capillary-sample setup. The electrical characterization of the Si wire is on a 4-point stage using the Hewlett-Packard (HP) 4155A Semiconductor Parameter Analyzer. The surface smoothness of the Si wire is characterized with Digital Instruments Veeco Dimension 3100 AFM and the data is processed in the Nanoscope Analysis software (v1.40) from Bruker Corporation.

Chapter III Fiber Structure Variance

3.1 In-silica optoelectronic fibers

Introduction

Recent advances in materials processing have enabled the fabrication of optoelectronic devices within Fibers, opening the path towards large-area, flexible device architectures that can be incorporated into fabrics. A number of approaches have been developed to realize in-Fiber optoelectronic devices. The first is based on prefabricated hollow Fibers[16,17,92], which are essentially used as a substrate for the subsequent infiltration or deposition of semiconductor material on their internal surface[13,93–99]. Another approach is based on well-established Fiber drawing techniques, in which a macroscopic version of the targeted multimaterial micro- or nano-structure containing all of the desired materials is fabricated and subsequently thermally scaled down to the desired dimensions[5,12,100–109]. The seamless integration of a range of co-drawable glassy semiconductors, metals and polymers has led to the fabrication of a rich variety of Fibers with functionalities spanning from optics to optoelectronics[110–112], albeit limited in their performance due to the amorphous nature of the semiconducting materials employed. Can the scalability of the thermal-drawing process be harnessed to fabricate similar in-Fiber optoelectronic microdevices using high performance semiconductors such as silicon or germanium? This possibility has thus far seemed unlikely, since the thermal drawing of crystalline materials requires their liquefaction, which in turn precludes the making of functional structures with

adjacent crystalline domains, lest they mix during the draw process and subsequently lose their predefined functionalities.

In this paper, we establish a fabrication method which yields optoelectronic devices positioned along a silica Fiber by integrating for the first time crystalline semiconducting material and metal electrodes in a precisely defined metal-semiconductor-metal architecture. To achieve this unprecedented results, two key challenges have been overcome, using a two-step approach. First, careful materials selection and fine-tuning of the drawing process enabled the co-drawing of in-silica Fiber crystalline semiconductor and metals at a temperature of about 2000°C while preventing mixing or inter-domain diffusion of the liquefied materials as well as shattering of the resulting Fiber upon cool-down (due to the mismatch of materials' temperature coefficients). This is achieved by maintaining a wide-enough silica-barrier between liquid domains at all times during the drawing process. The second challenge arises as physical and electrical contact must be established between the silica-separated metal and semiconducting domains that result from the first step, while continuing to prevent any uncontrolled collapse of the Fiber structure. To do so, the second step of our method harnesses a fluid instability phenomenon in Fiber drawing[113–115], which is related to the Plateau-Rayleigh capillary instability (PRI), the natural tendency of fluid cylinders to break up into spheres[116,117]. The selection of materials which have distinct melting points coupled with the proper choice of breakup temperature allows for only one domain to experience the fluid instability while the other is not impacted. This step, in which the semiconducting core is selectively broken up into a series of larger spheres, results in direct contacts between semiconducting spheres and

two continuous metal wires. The ladder-like final structure not only forms an integrated device in a single silica Fiber that exhibits measurable photosensitive properties, but also dramatically increases the density of functional components over the entire Fiber length when compared to previously achieved continuous-core photosensitive Fibers.

Fiber fabrication and Selective-breakup

The initial step in the making of integrated optoelectronic devices in a silica Fiber, relies on the so-called preform-to-Fiber fabrication technique, in which a macroscopic version of the desired structure (the "preform") is constructed using custom-developed glass processing technique and subsequently scaled down to the microscopic dimensions via thermal drawing. The top-left of Fig. 1a. schematically illustrates this step as well as the cross-sectional structure and composition of the preform. As previously mentioned, the choice of materials is paramount in the success of both the initial thermal-drawing and the subsequent controlled capillary breakup steps. Since the latter naturally calls for the use of a high melting temperature of the metal domains, we choose platinum (Pt) (melting point: 1,768 °C) as electrode material. Similarly, in order to maximize the difference in melting temperature between metallic and semiconducting domains, we favour doped germanium (Ge) (melting point: 938 °C) as semiconducting core material over silicon (Si) (melting point: 1,414 °C). Moreover, doped Ge has a smaller bandgap, greater near-infrared quantum efficiency and higher carrier mobility than Si[118]. A triple-core preform which contains two Pt 1 mm-diameter rods flanking a central Ge 0.8mm-diameter rod. Both Pt and Ge are crystalline materials, exhibiting both low viscosities and high diffusivities when

molten during the thermal drawing. These characteristics lead to an uncontrollable inter-domain mixing and diffusion if Pt and Ge are defined to contact with each other in the preform and to engage during the drawing process[119]. To keep the constituent materials separated during the draw, a viscous silica barrier is intentionally introduced between the cores of this two-material triple-core structure at the preform level by confining all the rods in separate silica tubes, which are arranged in a row with 1 mm-wide separations as illustrated in Fig. 1a. The preform is further cladded with concentric silica tubes to thicken the cladding up to a total outer diameter of 15 mm for proper structural support during the draw. The empty space inside preform is filled up with thin silica rods, and the entire assembly is sealed from both ends under vacuum to prevent oxidation of functional materials during the drawing process. The challenge of drawing such a structure lies in maintaining the integrity and symmetry of multiple cores down to the final scale while preventing the deformation caused by fluidic instabilities that can occur when the silica cladding is too soft and the Pt and Ge cores are in liquid phase. To prevent that, the preform is loaded in a Fiber draw tower and thermally drawn into a Fiber at the relatively low temperature of 2000 °C at which the silica remains viscous enough to provide a structural support to the liquid cores. The optical microscope image in Fig. 1b depicts the cross section of the resulting Fiber structure, where the Ge core in the center is surrounded by two Pt electrodes with silica barriers in between. The diameters of Ge core and Pt electrodes are scaled down to about 40 μm and 50 μm, respectively. This scale-down ratio is controlled by varying the Fiber draw to preform feed speeds ratio.

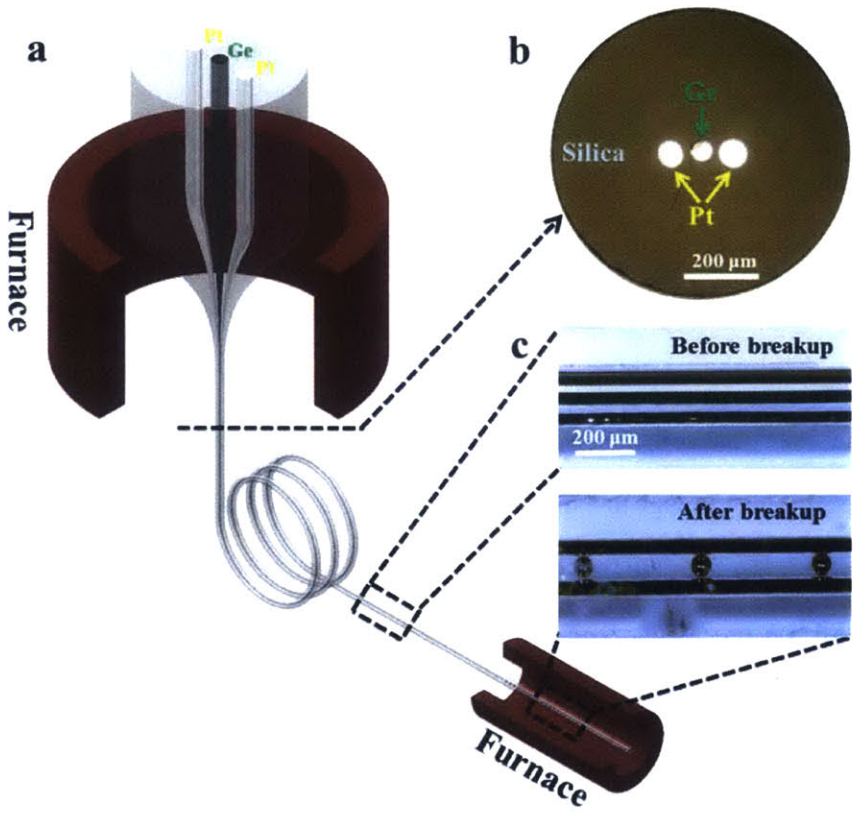

Figure III.1 **Fabrication and selective-breakup**

a, Schematic representation of the thermal drawing of a triple-core Fiber and after-draw selective breakup process in a heating furnace. **b**, Optical microscope image of the obtained Fiber cross-section. The resulting silica-cladding Fiber has three cores: one semiconductor (germanium) core in the middle and surrounded by two metal (platinum) cores. **c**, Side views of the triple-core Fiber before and after the selective breakup process.

Following the draw, the resulting Fiber is heated to selectively induce the PRI at the semiconductor region along the entire Fiber length while keeping the metal wires intact. At elevated temperature, an axially-uniform viscosity change along the Fiber length facilitates the breakup of the cylindrical core into discrete spheres as a result of core-

cladding interfacial energy minimization principle. Linear break-up of the continuous semiconductor core into periodic structure of discrete spheres, with a wavelength corresponding to the fastest instability growth rate. The size of spheres is thus dictated by the core diameter and the cladding viscosity contrast, which is a direct function of the applied temperature. To break up the Ge core into spheres while leaving the Pt electrodes intact, the breakup processing temperature should satisfy the following conditions: 1) it should be higher than the melting point of Ge to initialize the fluid instability, 2) it should be above the silica glass softening temperature of 1683 °C to decrease the viscosity contrast between Ge and silica enough to induce perturbations with reasonably fast growth rate, and 3) it should be lower than the Pt melting point to preserve the fixed wire shape of the Pt electrode. All the processing temperatures are indicated in Fig. 2, where the breakup temperature range satisfying the conditions above is indicated by the red shaded region. In this case, after drawing, a 10-cm long section of Fiber is kept inside a furnace for 40 minutes at a constant temperature of 1750 °C. At this temperature, the Ge core is in a low-viscosity liquid state and the silica cladding is at the lowest achievable viscosity without melting the Pt electrodes. Only the Ge core is thus influenced by the fluid instability and breaks up into a chain of Ge spheres with the diameters of around 110 μm, while Pt electrodes remain unperturbed. Due to the fact that the sphere diameter D_s is always larger than the diameter of the core from which it breaks D_c ($D_s = (3/2PD_c^2)^{1/3}$, where P is the particle spacing, and according to the Rayleigh condition $P > pi*D_c$[116,117]), the PRI-induced Ge spheres push the silica barriers aside and come in contact with the two solid Pt electrode wires, forming a ladder-like structure. The side view images of the Fibers before and after the selective breakup process are shown in Fig. 1c. This directed physical self-assembly

process breaks the axially-invariant topological structure inside the Fiber and allows the simultaneous formation of periodic and discrete in-Fiber electrical contact between crystalline semiconductor and metal materials, leading to an integrated optoelectronic multisensory device in silica Fiber. Additionally, the density of in-Fiber integrated components per unit length is dramatically increased by this selective breakup process, in which one cylinder device breaks into electrically addressable spherical devices linearly frozen in place within the silica cladding. The density can be further increased either by reducing the size of triple-core structure or by integrating multiple groups of triple-core structure within a single Fiber.

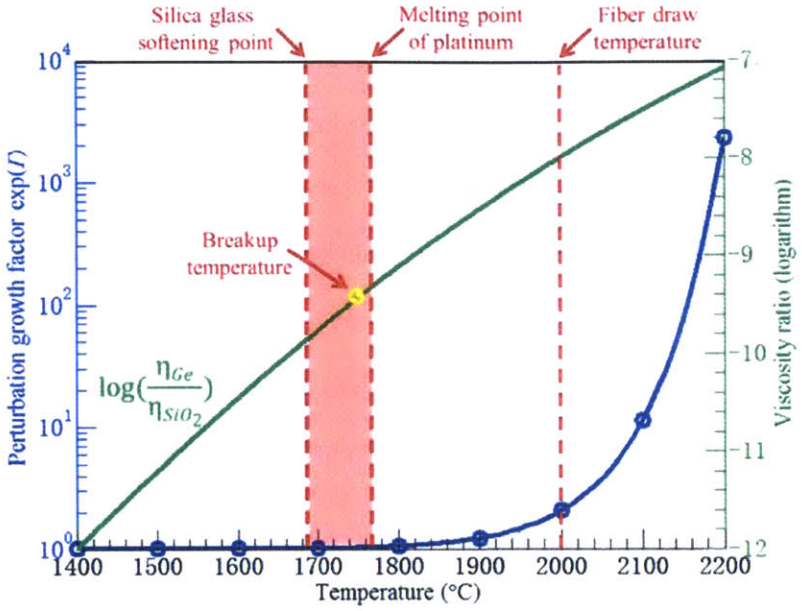

Figure III.2 **Choosing the selective-breakup process parameters**

Viscosity contrast of Ge/SiO_2 (green curve) and perturbation growth factor, exp(Γ) (blue curve with calculated points marked by blue circles) as a function of temperature. All the processing temperatures are indicated, including Fiber draw temperature of 2000 °C, breakup temperature of 1750 °C, silica glass softening temperature of 1683 °C, and Pt melting point of 1768 °C.

A capillary breakup is expected when a perturbation starts to grow such that its amplitude becomes comparable with the correspondent Fiber diameter. Different wavelengths of perturbations grow at different rates. To estimate the perturbation amplitude growth factor of the Ge core in a silica cladding, we consider a perturbation with wavelength of λ and use the Tomotika model that considers two infinite concentric cylinders to calculate the growth rate of the amplitude perturbation[120]. The growth rate, according to the Tomotika model, is a function of the viscosity ratio between Ge and silica, and of the Ge core diameter D_c. Both the viscosity ratio and the Fiber core diameter vary

significantly within the furnace heating zone: due to the drawing tension and the high temperature the preform is deformed into a thin Fiber and a "neck-down" shape is formed. As a result, the perturbation growth rate varies accordingly along the heating zone. By integrating the perturbation growth rate over the time the perturbation spends in the heating zone, the ratio between the final and the initial perturbation amplitudes, which is defined here as the perturbation growth factor, can be calculated. Figure 2 describes the viscosity contrast of Ge/SiO_2 (green curve) as a function of temperature[121–123], and the dependence of the calculated perturbation growth factor on the furnace temperature for a perturbation wavelength of λ = 1 cm. The loading and the drawing speeds in the calculation are set similar to their experimental values: 2 mm/min and 900 mm/min, respectively. The theoretical results are consistent with our observations in showing that capillary breakup can be avoided during the fiber draw process, while the selective breakup of Ge core during the reheating process remains possible with sufficient processing time, since the perturbation wavelength with the fastest growth rates sets the observed breakup period, which could be smaller than the processing time if the processing time is long enough.

Optoelectronic device based on selective-breakup

Beyond its simple visual observation, the realization of in-Fiber direct contact between crystalline semiconductor and metal electrodes is further confirmed by applying a bias voltage across the two Pt electrodes of a section of Fiber. As seen in Fig. 3a, the current response is imperceptible at this microampere scale before the selective process, which is in an open circuit status as expected. After the selective breakup process,

measurable current is induced by the applied voltage, and the nearly linear relationship between the two indicates the presence of ohmic contacts between Ge spheres and Pt electrode wires. The in-Fiber electrode scheme achieved here allows for robust electrical contacts with external circuits on either the end-facets or the side of Fiber, and thus no further metal deposition process is required.

As a photosensitive element, the Ge rod used in the preform is n-type with the doping concentration in the order of 10^{17} cm^{-3}. To investigate the optoelectronic performance in the resulting Fiber configuration, a 1550 nm laser diode with the maximum output power of 130 mW is used to illuminate the Ge spheres. The Pt electrodes which interface with Ge spheres along the entire Fiber length are connected to an external circuit. The Ge spheres undergo a change in electrical conductivity when externally illuminated[124], and a change in slope of the current-voltage (I-V) curve is obtained with respect to dark conditions, as plotted in Fig. 3a. A small non-linearity of I-V characteristics is also observed, and the reason is attributed the doping concentration of Ge rod which is not high enough to form perfect Ohmic contacts with the Pt electrodes. The optical bandwidth of the resulting Fiber is measured to be 470 kHz under a driving voltage of 3 V by modulating the input 1550 nm laser, as shown in Fig. 3b, which is three orders of magnitude higher than previously reported Fiber-integrated optoelectronic devices made by glassy semiconductors[5,12]. The rise time is measured to be on the order of microseconds, as illustrated in the inset of Fig. 3b. High-performance optoelectronic devices require high-quality semiconductors as the functional materials and junctions as the fundamental components. Therefore, further development in in-Fiber material processing and the

realization of in-Fiber junction is expected to lead to improvements in device performance. For example, with the recent demonstration of the formation of rectifying p-n junctions in silicon-in-silica Fibers by HPCVD process, bandwidth of up to 3 GHz and rise time of picoseconds can be achieved[13]. Moreover, changing the composition of the semiconductor core can adjust the spectral characteristics of the photoconductive response[125,126]. For instance, the realization of Si-Ge heterojunction can significantly improve the efficiency and speed of in-Fiber integrated optoelectronic devices.

We further study the dependence of the device performance on the sphere diameter. To generate Ge spheres with smaller diameters, we first reduce the Fiber sizes using a high-tension low-ratio downscaling process to prevent any process-induced fluidic instabilities. An initial Fiber with the same dimensions as the one shown in Fig. 1a is chosen, which has a Ge core with diameter of 40 μm and two Pt wires with diameter of 50 μm. The downscaling process starts with a slow feeding speed of 3 mm/min and a relatively fast drawing speed of 15 mm/min under high tension in a hydrogen flame. A scaling factor of $\sqrt{5}$ is therefore obtained. We repeat the process twice, and the resulting diameters of Ge core after the first and second tapering processes are about 18 μm and 8 μm, as the side views shown in Fig. 4a and 4b, respectively. The same selective breakup approach is then applied separately to the resulting Fibers from both tapering processes, leading to the formation of smaller Ge spheres connected with Pt electrodes, as illustrated in Fig. 4a and 4b. The breakup time for each process step is shortened due to the reduced sizes of Ge cores, but the breakup temperature is maintained at 1750 °C. The diameters of the resulting Ge spheres in Fibers after the first and second tapering processes are around 48 μm and 21

μm, respectively, which are further confirmed by releasing spheres from the silica Fibers using hydrofluoric acid and analyzing dimensions using a scanning electron microscope (SEM). The device performance of the resulting Fibers with different sphere sizes is then characterized with the illumination of a 1550 nm laser and a 1310 nm laser, as illustrated in Fig. 4c. Higher photosensitivity is observed with the illumination wavelength of 1550 nm than 1310 nm, which is due to the fact that the photoresponsivity of Ge at 1550 nm is higher than that at 1310 nm[124]. In our case, the dark current I_{dark} is defined as the average current in the Fiber when no photons are incident on it, and the photocurrent I_{light} is the average current under predefined illumination condition. I_{light} - I_{dark} is in fact inversely proportional to D_s^2 for fixed number of incident photons at a given wavelength, which is limited to the penetration depth of the incident wavelength[127,128]. The dependence of the photoconductance on the sphere size reveals that reducing the sizes of photoconducting Ge spheres can be an efficient way to enhance the photosensitivity. Moreover, attaining smaller diameters increase the Fiber mechanical flexibility while reducing the cost and weight of Fibers, thus allowing the realization of wearable and conformal smart fabrics.

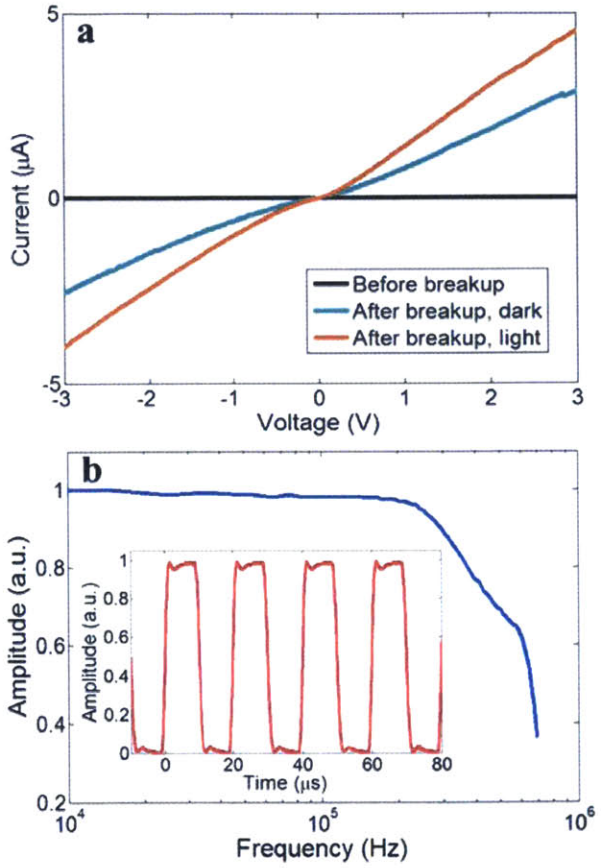

Figure III.3 **Optoelectronic device characterization**

a, Photoconductance of a triple-core Fiber before and after the selective breakup process in the dark and on the illumination of a 1550 nm laser. **b**, Optical bandwidth of the detector is measured to be 470 kHz. Inset: response time measurement of the resulting Fiber on the illumination of a modulated 1550 nm laser.

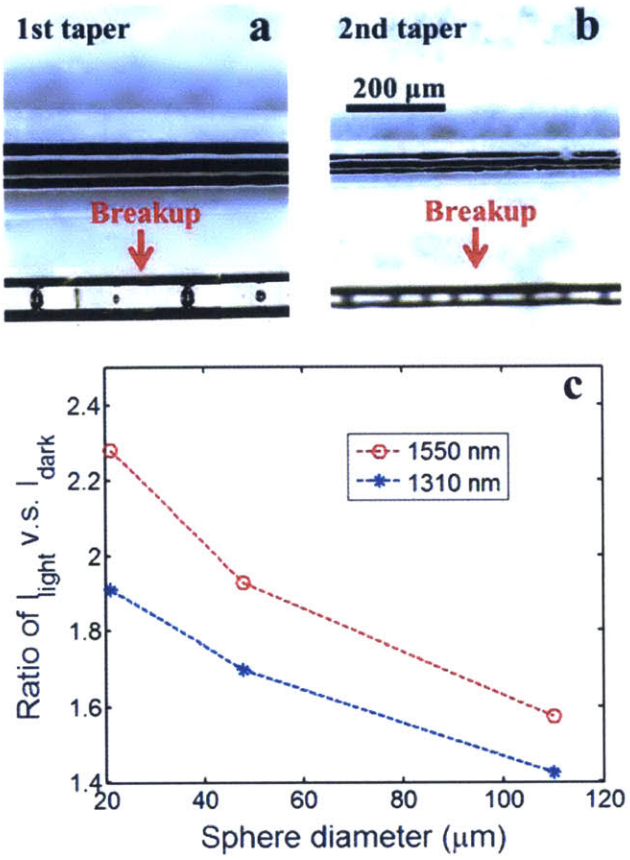

Figure III.4 **Tapering process and device characterization**

a-b, Side view of triple-core fibers before and after the selective breakup process after first and second tapering process using high-tension low-ratio downscaling method by a hydrogen torch. **c**, Photoconductance of the resulting fibers with different sphere sizes on the illumination of a 1550 nm laser and a 1310 nm laser.

Further improvement in process development and material quality is expected to achieve better device performance and broader functionalities. For example, the isothermal capillary breakup used here is known to frequently induce chaotic regimes where small "satellite" spheres are formed which do not contact metal electrodes[113,129]. To avoid chaotic

regimes, a gradual liquefaction of feeding Fiber into a fixed heating source can be used to induce the formation of monodisperse spheres. A laser heating source is also favourable to offer better control of processing temperature. Moreover, traces of oxygen in the semiconductor core due to the dissolution of the cladding glass in the molten core during the Fiber draw process limits the electrical properties of resulting devices. An *in situ* reactive getter of oxygen is an effective method to be included in Fiber draw process to achieve oxygen-free semiconductor core[76]. Last but not least, process induced stresses are capable of modifying the electronic band structure of the semiconductor material, which allows the fine engineering of optical detection range[95,130,131]. In general, since this fabrication approach relies on a physical breakup mechanism as opposed to chemical synthesis, it significantly broadens the repertoire of accessible materials and geometries. In-fact, the proposed fabrication process is highly versatile, allowing a variety of families of semiconductors that are sensitive to other physical parameters to be integrated in a single Fiber, for example, an energy-harvesting Fiber can be realized with the integration of thermoelectric core made by SiGe compound. The interplay between materials properties and structure integration in these Fibers provides us new opportunities to deliver novel semiconductor device functionalities at Fiber-optic length scales, uniformity and cost, leading to the realization of more sophisticated functionalities and the prospect of truly multifunctional Fibers.

3.2 Fiber surface patterning

Introduction

Surface patterning is a mature technique that have been used widely in decoration, photonics, plasmonics, biology, medical, etc[132–136]. Different techniques are used to treat various materials for different pattern feature. People use stamp printing or molding and embossing to create millimetre scale patterns while use e-beam lithography and scanning probe techniques for features in micron or nano scale[137,138]. The difficulty and cost of patterning the surface normally depends on the feature size and the patterned area size. As with the feature size goes smaller and smaller, the difficulty increases sharply and the cost correspondingly rises. In most cases, the pattern feature in millimetre scale could be fabricated in large scale for decoration purpose while the pattern feature in micron, nano scale for scientific purpose are normally fabricated in lab-scale both because of the time consuming and the cost associated with it. Fiber drawing technique is known for creating large-scale devices in a cost-effective way. A single preform would normally be drawn into hundreds of meters long, micron-scale diameter fiber. The inside of the fiber is thoroughly studied for different kinds of devices, while the fiber surface is seldom modified or studied. Most of the time, the fiber surface is kept smooth and clean to maintain the fiber mechanical strength.

Here we combine both techniques, the surface patterning and thermal fiber drawing, to generate a large-scale, micron or even nano scale feature surface in an efficient and cost effective way. The combination of surface patterning and thermal fiber drawing inherit the

advantage side from both techniques and could be widely adapted. Firstly millimetre scale feature on the fiber preform could be fabricated using different common pattern technique depending on the materials selected. After the surface patterning on the preform surface, the preform is sent to go through the thermal drawing and get elongated. The parameter of the thermal drawing including temperature, the feeding and drawing speed are carefully selected to maintain the surface structure shape while only allowing it to scale down accordingly. After drawing, the surface pattern size shrinks the same order as the size of the fiber, hence a millimetre scale pattern on a large preform surface would end up with a micron scale pattern on a fiber surface.

Fiber surface pattern technique

Figure III.5 illustrate how the patterning technique is combined with thermal fiber drawing. Three different pattern techniques are used to treat 3 different commonly used materials, as illustrated in Supplementary Figure III-1. In the first case, PC is a polymer that could be easily mechanically engineered and is therefore a good match with a milling machine. We use a piece of PC with 1.5" wide and 0.5" thick, and use the end mill to cut periodic trenches on the surface. The type of end mill and the period could vary depending on the designed structure. For example, a 0.5 millimetre diameter square-shape end mill cutting a bunch of 1 millimetre period trenches would result in a structure with 0.5 millimetre pillar and 0.5 millimetre trench. The preform is then drawn at a temperature of 260 °C with a feeding speed of 1mm/min and drawing speed of 2.5m/min. The ratio of the speeds determines the draw down ratio to be 50. Along with the draw down ratio of 50,

this would turn into a series of 10 micron pillar on a fiber and they're all 10 micron away from each other. Figure III.5(d) shows the SEM image of the resulting fiber. The surface pillars could be clearly seen both from the top side view and from the cross-section view.

In the second case, PMMA is another polymer that could both be mechanically engineered and cut with a laser. One advantage of laser is that it could quickly process the pattern task, however the shape of the pillar is not as rectangle as the one cut by end mills. The PMMA normally get burned the most on the surface and the deeper the laser goes the smaller region burned, which leave the pattern a triangle shape. The PMMA is drawn at 240 °C with similar speed setup. After drawing, the triangle shape is be maintained and the pillar size shrink with the same scale as the fiber. Figure III.5 (d, e) shows the resulting fiber surface.

In the third case, a piezoelectric material PVDF is also treated to get surface pattern and get drawn into fiber. The problem in this material is that it's crystalline and couldn't maintain the shape itself when heated up as other polymers behave during the draw. However the property that it doesn't stick with other materials helps making the surface-patterned fiber using a moulding method. The PC plate is again used and get pattern cut on the surface. The PVDF is then embedded between the PC plate and another non-treated PC plate. The whole structure is heated up to 180 °C to consolidate the structure. This temperature is slightly above the PC glass transition temperature so that PC only get softened a little bit. However it's much higher than PVDF's melting point so PVDF melt and fill the space between the pillars on the PC surface. The consolidated preform is then thermally drawn and the pillar array structure inside the preform is scaled down into micron

structure inside a PC-clad fiber. Since PC and PVDF doesn't stick with each other very well, the PC-clad fiber could be easily peeled into two parts, one containing the PC with surface patterned and the other containing the PVDF with surface patterned. In this way the PVDF is also successfully patterned on the surface with micron-scale features. Figure III.5 (f) shows the surface SEM image of the pattern on the PVDF surface and Figure III.5 (g) shows the pattern of the PC on the other piece of the peeled fiber.

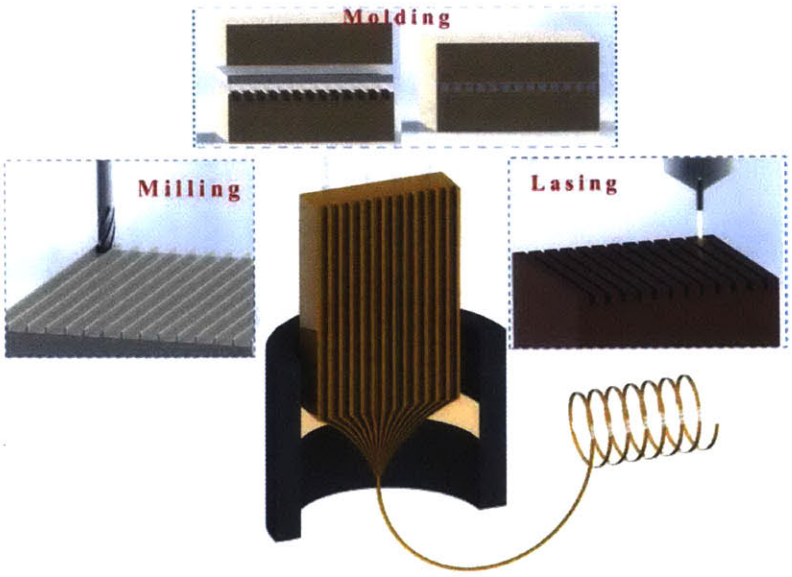

Supplementary Figure III-1 **Combining surface pattern techniques and thermal fiber drawing**

Different patterning techniques that we used to create patterns on the preform surface including milling, laser cutting, and molding. The patterned preform is then sent to go through the thermal drawing process in a hot furnace to get long and small fibers.

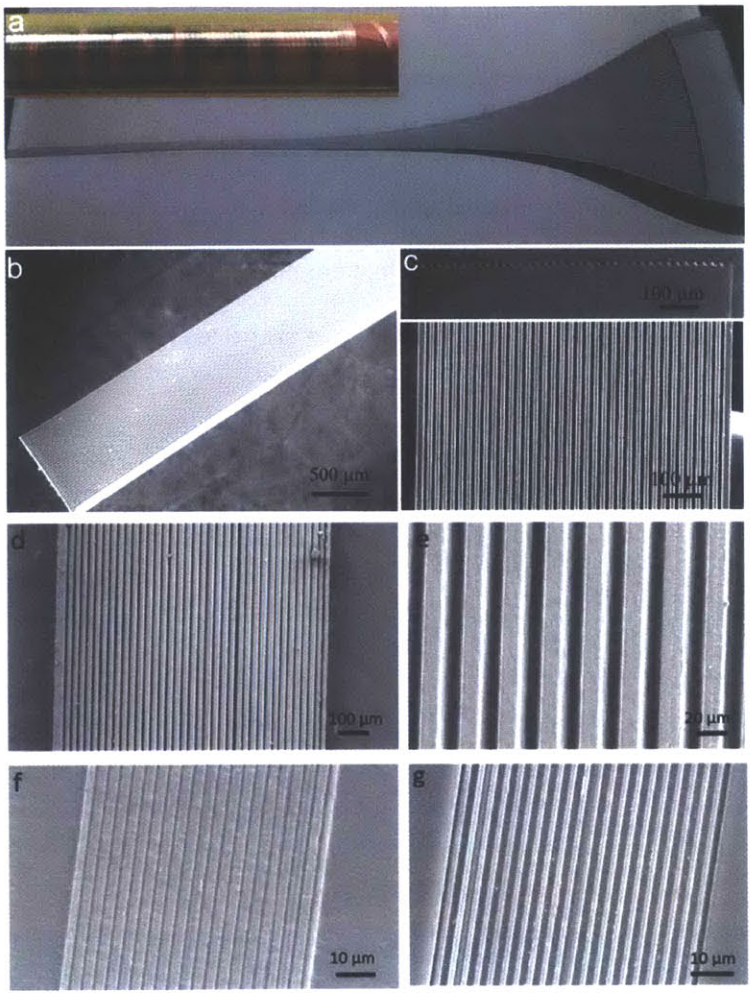

Figure III.5 **Different material fiber surface fabricated from different methods**

a, The preform residual after a fiber drawing. The inset shows the fiber surrounding a pensil. **b-c**, the SEM images of a PC fiber. The inset shows the cross section image of the surface patterns on the fiber. **d-e**, the SEM images of a PMMA fiber from top view. **f,** pattern on the surface of PVDF. **g**, pattern on the surface of PC which is contacting the PVDF before peeling off.

Because of the multiple choices among the materials and the tools to pattern the surface of the preform, the surface could be patterned in a lot of different ways. Figure III.6

illustrate several of them including designing hierarchical structure on the fiber surface, generating different pillar with or trench with for the surface pattern, and getting the nano-scale pattern on the fiber surface.

Figure III.6 (a, b) shows a hierarchical structure on the fiber surface. There are 6 wide pillar on the fiber surface, each spanning around 50 um and 50 um away from each other. On top of these pillars, there are another layer of pillar array which are about 5um wide and 5um away from each other. The inset shows how one of pillar looks like from cross-section view. In order to make this pattern, the preform is firstly cut with a large diameter end mill to get the big pillars and then cut with a fine end mill for features on top of each pillar. Figure III.6 (c, d) illustrate that on the same fiber surface, the width of the pillar and the trench could be both tuned. In Figure III.6 (c), a series of different width pillar is spaced the same distance from each other, while in Figure III.6 (d), the pillar size are kept the same while their distance goes from sub-micron to as large as 10 micron. This kind of pattern could easily be designed and fabricated on the milling machine and get drawn into fiber while maintaining the feature aspect ratio. Lastly we show that sub-micron scale feature on the fiber surface could also be achieved. Because thermal fiber drawing needs to heat up the materials to get viscosity, the features on the surface inevitably deform to some extent, and the larger the draw down ratio the larger deformation. So usually when the feature goes to sub-micron scale, the pillar melt and spread too much to be seen evidently. Although this effect could be compensated by running through some air flow on the surface during the drawing, it's still hard to achieve the nano-scale feature in one draw. Supplementary Figure III-2 compares the shape of the pillars for micron-scale and sub-

micron scale. As can be seen, the sub-micron width pillars are associated with low height while the larger width pillar's profile is much sharper. In order to get sub-micron scale feature while maintain the sharp profile, we use a re-draw method in which we first draw a fiber with around 20 um pillar size and then put the fibers together in an array on top of another preform and do the thermal drawing again. With the draw down ratio relatively low for both processes, we can get much better profile when scale goes down to sub-micron. Figure III.6 (e-f) shows how the final fiber and the fine pillar looks like. There are around 20 sub-fiber on the final fiber and each sub-fiber has around 60 pillars. In this way, a fiber with more than 1000 sub-micron-size pillars is fabricated.

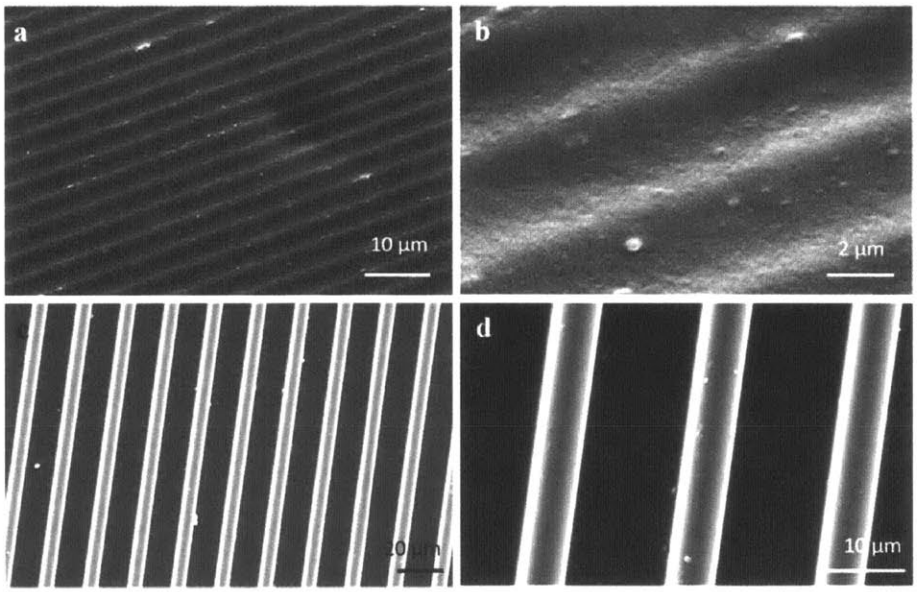

Supplementary Figure III-2 **Comparison between sub-micron scale pillar and micron scale pillar profile**

a-b, the pillar half-height width is around 700 nm, while the pillar height is much decreased. **c-d**, the pillar half-height width is around 5 um, and the pillar profile is sharp according to the SEM images from the top view.

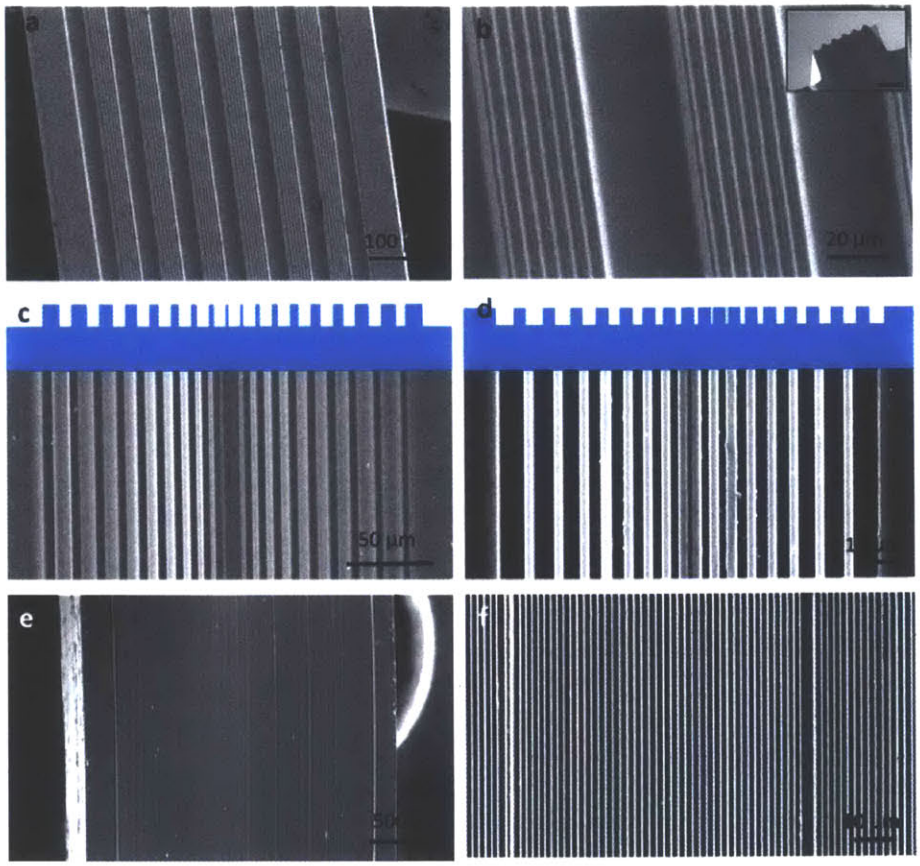

Figure III.6 **Tuning the fiber surface patterning**

a-b, a fiber with hierarchical structure on the surface. There are 6 wide pillars on the fiber surface, each containing another small pillar array on their top side. The inset is the cross section view of one of the big pillars. scale bar in inset is 20 um. **c-d**, the fiber surface could be designed with different pillar size (left) and different trench size (right). The top model illustrate the design of the surface pattern. **e-f,** the fibers with surface patterned are put in an array on top of another perform and further drawn to get nano-scale feature.

Discussion on fiber surface pattern properties

Since the pattern techniques result in uniform features on the preform surface and the scale-down process keeps the draw-down ratio almost the same everywhere on the

surface, the feature on the final fiber is therefore kept uniform both in large pillar case and in sub-micron scale pillar case. Figure III.7 shows the fiber surface pillars' image as well as the statistics of their width. For both cases, the fiber sample is taken every 1 meter over 5 meters range. After the SEM image from top view for all the samples are taken under the same condition, the pillars' width is measured with the help of the software ImageJ. From the width distribution, the pillar width is uniform with a small variance, 1.3% for larger pillar case and 4% for sub-micron pillar case respectively.

The uniformity of the pillar size gives rise to the coloration phenomenon when the pillar size is comparable to the visible light wavelength. Shown in Figure III.8 (a-d) is how the fiber exhibits different color when viewed from different angle. The reason for this could be explained by simply looking at the grating diffraction equation:

$$d(sin\theta_i - sin\theta_m) = \pm m\lambda, \quad m = 0,1,2,\cdots \qquad \text{Equation III-1}$$

In the above equation, d is the distance between the pillars, θ_i is the incident angle, θ_m is the angle corresponding to m'th order of diffraction. The intensity for the wavelength λ reach maximum at the angle θ_m.

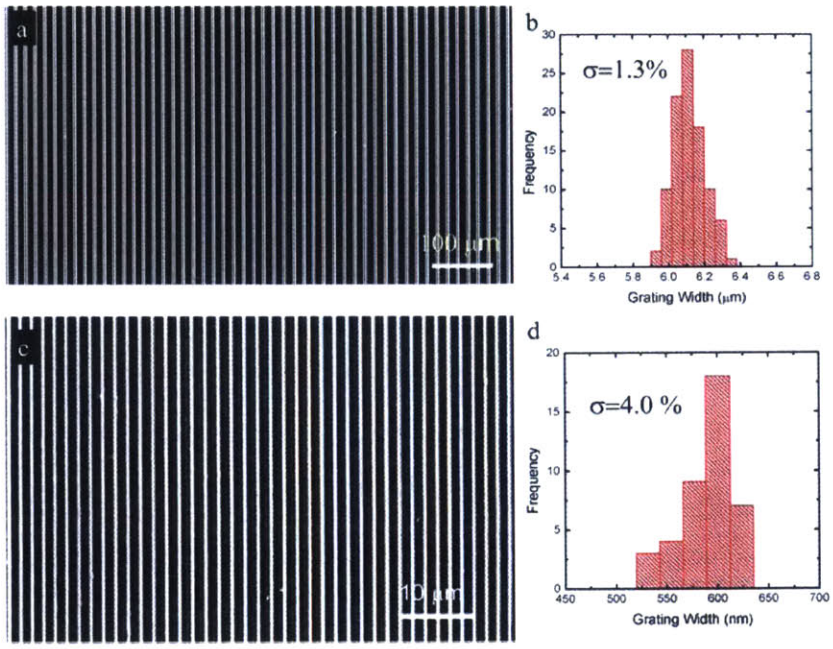

Figure III.7 **Pillar size uniformity**

a, fiber from 1st draw, the pillar width is about 6 um. **b**, statistics of the pillar width with samples taken from over 5 meter long range. **c**, fiber from redraw process, the pillar width is about 500 nm. **d**, statistics of the pillar width with samples taken from over 5 meter long range.

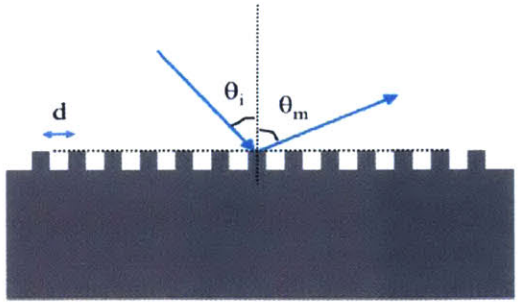

Supplementary Figure III-3 **Illustration of diffraction on fiber surface**

This figure illustrate the incident angle and the diffraction angle on the surface. The surface is grated with period of d. Note that if θ_m is on the same side of the perpendicular dashed line as θ_i. θ_m should be negative in the above formular.

The multi-channel, micron to sub-micron scale feature on the fiber surface also enhances the hydrophobic properties in the direction across the fiber. As seen from Figure III.8 (e-g), the contact angle between the droplet and the fiber surface varies among different alignment and different surfaces. The surface patterned PC fiber is first aligned side by side and consolidated to make one wide piece for measurement. The formed piece maintains the micron size pillars on one side. On the side with the multiple micron size pillars, the contact angle along the fiber direction is 90°, about the same as that on the smooth side of the fiber. However the contact angle across the fiber is 148°, much larger than the smooth surface. The comparison shows the huge improvement on the hydrophobic property across the fiber surface micron size pillars while along the fiber direction the hydrophobic property is about the same as the untreated surface. This anisotropic hydrophobic property induces directional wetting on the fiber surface. Liquid could flow along the fiber but won't interfere each other when they're confined in between of different pillars, as shown in Supplementary Figure III-4.

The surface patterned fiber could be further processed to get periodic structure along both directions. A piece of silicon wafer is used as the stamp and first get etched to have 7.5 um wide trenches and 7.5 um wide pillars. This piece of wafer is then pushed on top of the surface patterned PC fiber while the direction of the channel on the wafer is perpendicular to the channels on the fiber. The fiber is also heated up to 140 °C to help the stamping process. After 30 minutes, the fiber with 2 dimensional periodic structure is achieved, as shown in Figure III.9. The depth of the stamp relates to the temperature, the stress, and the time of stamping. With a stronger stress the notch on the pillar could go

deeper. The stamping process time could also be shortened with a stronger stress and higher temperature.

To conclude, the method of combining the normal surface pattern technique and the thermal fiber drawing is an efficient and low cost way to create micron to nano scale pattern over a large area. This method is versatile, as different surface pattern techniques could be used in this method to treat different types of materials. With appropriate parameters, the thermal drawing process scales down the features on the surface along with the fiber while maintain their profiles. The resulting fiber has a lot of potential applications in different area. It could show various color when viewed from different angle when the pattern size is comparable to the visible light wavelength. The surface, because of the multiple micron pillars, also demonstrates anisotropic hydrophobic property which could be used for directional wetting applications. Last but not least, the surface patterned fiber could be easily further processed to achieve 2 dimensional periodic structure by stamping. This work expands the functional area of the fiber from inside to outside and yynergy of the fiber surface pattern and the inner structure could possibly create more advanced multi-functional fiber devices.

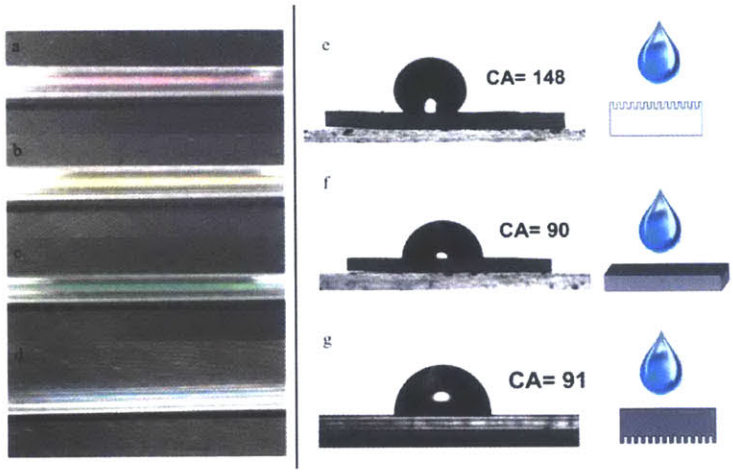

Figure III.8 **Fiber color and directional wetting**

a-d, images take from the same fiber with different angle. **e-g**, contact angle measurement with different configuration. On the right the model demonstrate how the fiber is placed when taking the measurement. In **e-g**, the fibers are aligned side by side and consolidated to form a wider piece to make sure the droplet not touch the edge. CA is short for contact angle and the number's unit is degree.

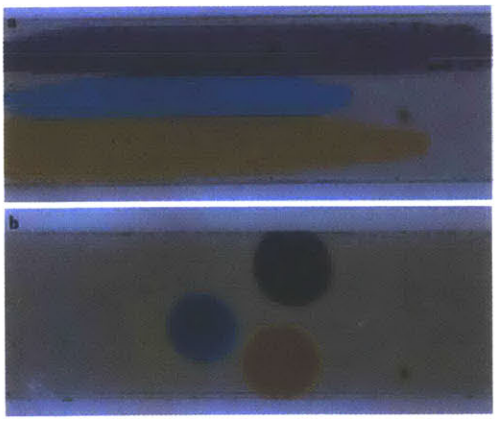

Supplementary Figure III-4 **Directional wetting on the patterned fiber surface**

a, on the side with the micron size pillars, the ink flows along the fiber. The pillars on the fiber surface confine the ink flowing across the fiber surface. **b**, on the side with no pattern, the ink stays and doesn't spread.

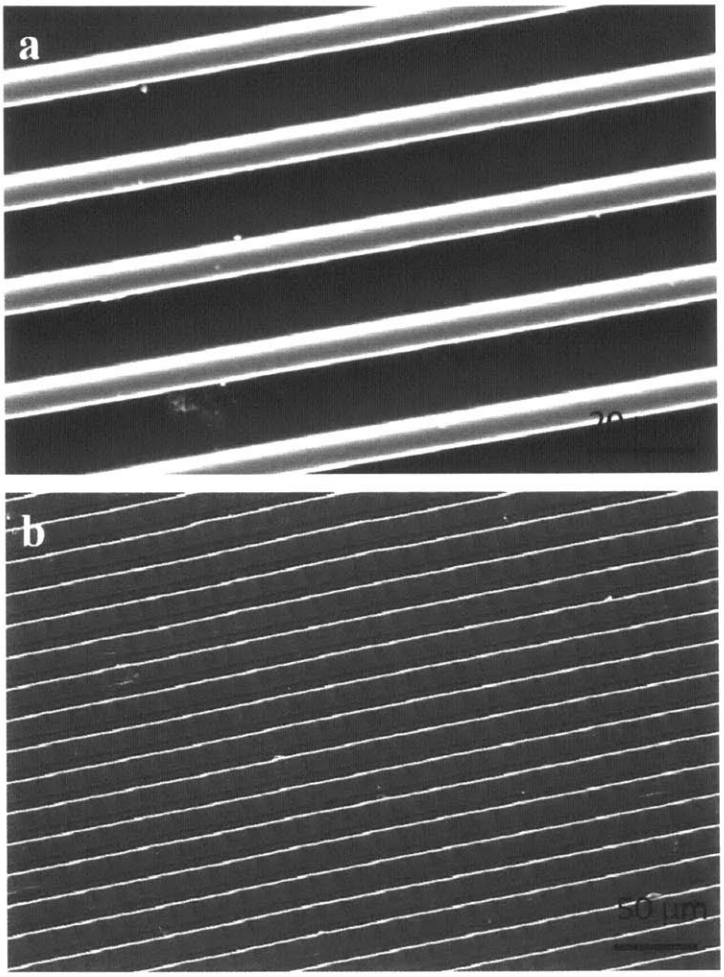

Figure III.9 **Surface patterned fiber, before and after perpendicular stamping treatment**

a, As drawn fiber with surface patterned with a series of pillars, the pillar width is about 10 um and the distance is about 15 um. b, the same fiber surface after a stamping treatment. A piece of pre-defined Si wafer (7.5 um wide pillar and 7.5 um pillar distance) is pushed on top of the fiber at a temperature of 140 °C for 30 minutes. The wafer is aligned such that the pillar on the wafer is perpendicular to the pillar on the fiber surface. The resulting fiber surface shows a "bamboo" structure.

Chapter IV Summary and Future Work

Through the above demonstrated projects, we see a much wider research area around multi-material, multi-functional fiber. From material perspective, not only the materials that have similar thermal property could be drawn together, but materials with distinct melting point could also be possibly bundled together in a fiber draw. And not only that different materials could be drawn, but new materials could even be fabricated through the draw. In this sense, the fiber is not only treated as a device but also a chemical reaction vehicle. The unique condition of the fiber draw, high temperature and high stress resulting from the scaling scheme, helps increasing the change of the materials engage and react. From the structure perspective, the fiber's inside symmetry in longitudinal is broken using the thermal breakup technique. The breaking symmetry, i.e. the formation of standalone spheres, could be possibly used to build high-density in-fiber devices. Also the fiber surface is studied and demonstrated to be engineered. With the example of fiber surface patterning, we see the potential of combining both the inner device inside the fiber and the outer surface structure.

Nevertheless, all the work are explorative and are not mature enough from the product point of view. Though in all the projects different applications based on the respective techniques are demonstrated, the performance of all those devices could be further improved. In order to get optimized structure and fully utilize the fiber drawing condition to promote the chemical reaction, a much deeper understanding of the fiber drawing condition and molecular interaction need to be established. In order to design the

most efficient device configuration inside fiber through thermal breakup, more parameters in the breakup condition should be tuned to search for the best suited setup. Meanwhile, a new heating method, i.e. the laser heat up, is being tested too. The laser heating setup could selectively heat up one part of the fiber hence giving a log of advantage in selective breakup. Correspondingly the associated parameter for laser heat up should be studied to find a proper condition for different material combinations.

All in all, the exploration shows that the limit of the multi-material, multi-functional fiber is much beyond what we're currently studying. This thesis work expands the playground for a new fiber technology platform that has the potential to impact a wide range of industries. Large area electronic and optoelectronic assemblies, functional fabrics, sensors with unprecedented functionalities, clean energy are among the most intriguing. Envisioned are fibers integrating thousands of devices and capable of even more complex functionalities in logic and detection operations. Development is underway to bring these concepts and devices to a higher level of maturity.

Bibliography

(1) Kvavadze, E.; Bar-Yosef, O.; Belfer-Cohen, A.; Boaretto, E.; Jakeli, N.; Matskevich, Z.; Meshveliani, T. *Science* **2009**, *325*, 1359.

(2) Kao, C. K. *Rev. Mod. Phys.* **2010**, *82*, 2299–2303.

(3) Stone, J. *Appl. Phys. Lett.* **1973**, *23*, 388.

(4) Richardson, D. J.; Nilsson, J.; Clarkson, W. A. *J. Opt. Soc. Am. B* **2010**, *27*, B63.

(5) Bayindir, M.; Sorin, F.; Abouraddy, A. F.; Viens, J.; Hart, S. D.; Joannopoulos, J. D.; Fink, Y. *Nature* **2004**, *431*, 826–829.

(6) Bayindir, M.; Abouraddy, A. F.; Arnold, J.; Joannopoulos, J. D.; Fink, Y. *Adv. Mater.* **2006**, *18*, 845–849.

(7) Danto, S.; Sorin, F.; Orf, N. D.; Wang, Z.; Speakman, S. a; Joannopoulos, J. D.; Fink, Y. *Adv. Mater.* **2010**, *22*, 4162–4166.

(8) Stolyarov, A. M.; Wei, L.; Shapira, O.; Sorin, F.; Chua, S. L.; Joannopoulos, J. D.; Fink, Y. *Nat. Photonics* **2012**, *6*, 229–233.

(9) Fink, Y.; Ripin, D. J.; Fan, S.; Chen, C.; Joannopoulos, J. D.; Thomas, E. L. *J. Light. Technol.* **1999**, *17*, 2039.

(10) Hart, S. D.; Maskaly, G. R.; Temelkuran, B.; Prideaux, P. H.; Joannopoulos, J. D.; Fink, Y. *Science* **2002**, *296*, 510–513.

(11) Shapira, O.; Kuriki, K.; Orf, N. D.; Abouraddy, A. F.; Benoit, G.; Viens, J. F.; Rodriguez, A.; Ibanescu, M.; Joannopoulos, J. D.; Fink, Y.; Brewster, M. M. *Opt. Express* **2006**, *14*, 3929.

(12) Abouraddy, A. F.; Bayindir, M.; Benoit, G. *Nat. Mater.* **2007**, *6*, 336–347.

(13) He, R.; Sazio, P. J. A.; Peacock, A. C.; Healy, N.; Sparks, J. R.; Krishnamurthi, M.; Gopalan, V.; Badding, J. V. *Nat. Photonics* **2012**, *6*, 174–179.

(14) Senior, J. M. *Optical Fiber Communications: Principles and Practice*; Prentice-Hall International Series in Optoelectronics; Prentice Hall: New Jersey, 1985.

(15) Agrawal, G. P. *Fiber-Optic Communication Systems*; Wiley Series in Microwave and Optical Engineering; Wiley, 2010.

(16) Knight, J. C. *Nature* **2003**, *424*, 847–851.

(17) Russell, P. *Science* **2003**, *299*, 358–362.

(18) Abouraddy, A. F.; Bayindir, M.; Benoit, G.; Hart, S. D.; Kuriki, K.; Orf, N.; Shapira, O.; Sorin, F.; Temelkuran, B.; Fink, Y. *Nat. Mater.* **2007**, *6*, 336–347.

(19) Egusa, S.; Wang, Z.; Chocat, N.; Ruff, Z. M.; Stolyarov, A. M.; Shemuly, D.; Sorin, F.; Rakich, P. T.; Joannopoulos, J. D.; Fink, Y. *Nat. Mater.* **2010**, *9*, 643–648.

(20) Snitzer, E.; Tumminelli, R. *Opt. Lett.* **1989**, *14*, 757.

(21) Morris, S.; Hawkins, T.; Foy, P.; McMillen, C.; Fan, J.; Zhu, L.; Stolen, R.; Rice, R.; Ballato, J. *Opt. Mater. Express* **2011**, *1*, 1141.

(22) Orf, N. D.; Shapira, O.; Sorin, F.; Danto, S.; Baldo, M. A.; Joannopoulos, J. D.; Fink, Y. *Proc. Natl. Acad. Sci.* **2011**, *108* , 4743–4747.

(23) Ballato, J.; McMillen, C.; Hawkins, T.; Foy, P.; Stolen, R.; Rice, R.; Zhu, L.; Stafsudd, O. *Opt. Mater. Express* **2012**, *2*, 153.

(24) Matsuoka, T. *Adv. Mater.* **1996**, *8*, 469–479.

(25) Sou, I. K.; Ma, Z. H.; Wong, G. K. L. *Appl. Phys. Lett.* **1999**, *75*, 3707.

(26) Gavrushchuk, E. M. *Inorg. Mater. 39*, 883–899.

(27) Sorokina, I. T. *Opt. Mater. (Amst).* **2004**, *26*, 395–412.

(28) Zimmer, J. P.; Kim, S.-W.; Ohnishi, S.; Tanaka, E.; Frangioni, J. V; Bawendi, M. G. *J. Am. Chem. Soc.* **2006**, *128*, 2526–2527.
(29) Mirov, S.; Fedorov, V.; Moskalev, I.; Martyshkin, D.; Kim, C. *Laser Photon. Rev.* **2010**, *4*, 21–41.
(30) Sparks, J. R.; He, R.; Healy, N.; Krishnamurthi, M.; Peacock, A. C.; Sazio, P. J. A.; Gopalan, V.; Badding, J. V. *Adv. Mater.* **2011**, *23*, 1647–1651.
(31) Krishnamurthi, M.; Barnes, E.; Sparks, J. R.; He, R.; Baril, N. F.; Sazio, P. J. A.; Badding, J. V.; Gopalan, V. *Appl. Phys. Lett.* **2012**, *101*, 021108.
(32) Kimura, H.; Komiya, H. *J. Cryst. Growth* **1973**, *20*, 283–291.
(33) Okamoto, H. *J. Phase Equilibria* **1997**, *18*, 676–676.
(34) He, R.; Day, T. D.; Krishnamurthi, M.; Sparks, J. R.; Sazio, P. J. A.; Gopalan, V.; Badding, J. V. *Adv. Mater.* **2013**, *25*, 1461–1467.
(35) Gumennik, A.; Stolyarov, A. M.; Schell, B. R.; Hou, C.; Lestoquoy, G.; Sorin, F.; McDaniel, W.; Rose, A.; Joannopoulos, J. D.; Fink, Y. *Adv. Mater.* **2012**, *24*, 6005–6009.
(36) Current, M.; Gilder, H. M. *Phys. Rev. B* **1977**, *16*, 2386–2391.
(37) YU, P.; Cardona, M. *Fundamentals of Semiconductors: Physics and Materials Properties*; Advanced texts in physics; Springer Berlin Heidelberg, 2005.
(38) Hotje, U.; Rose, C.; Binnewies, M. *Solid State Sci.* **2003**, *5*, 1259–1262.
(39) Lucovsky, G. *Phys. Status Solidi* **1972**, *49*, 633–641.
(40) Yang, K.; Cui, Q.; Hou, Y.; Liu, B.; Zhou, Q.; Hu, J.; Mao, H.-K.; Zou, G. *J. Phys. Condens. Matter* **2007**, *19*, 425220.
(41) Nesheva, D.; Scepanovic, M. J.; Askrabic, S.; Levi, Z.; Bineva, I.; Popovic, Z. V. *ACTA Phys. Pol. A* **2009**, *116*, 75–77.
(42) Taylor, W. *Phys. Lett. A* **1967**, *24*, 556–558.
(43) Guinebretière, R. *X-ray Diffraction by Polycrystalline Materials*; ISTE: London, UK, 2007.
(44) Kubaschewski, O. *Materials thermochemistry /*; Pergamon Press,: Oxford ;, 1993.
(45) Deng, D. S.; Orf, N. D.; Danto, S.; Abouraddy, A. F.; Joannopoulos, J. D.; Fink, Y. *Appl. Phys. Lett.* **2010**, *96*, 023102.
(46) Abbott, P.; Sosa, E. D.; Golden, D. E. *Appl. Phys. Lett.* **2001**, *79*, 2835.
(47) Swank, R. K. *Phys. Rev.* **1967**, *153*, 844–849.
(48) Orf, N. Multimaterial rectifying device fibers, 2009.
(49) Pierret, R. F. *Semiconductor device fundamentals : [with computer-based exercises and homework problems]*; Addison, Wesley, Longmann: Reading, Mass. [u.a.], 2003.
(50) Samantilleke, A. P.; Boyle, M. H.; Young, J.; Dharmadasa, I. M. *J. Mater. Sci. Mater. Electron.* *9*, 231–235.
(51) Dresselhaus, G.; Kip, A.; Kittel, C. *Phys. Rev.* **1955**, *98*, 368–384.
(52) Klement, W.; Willens, R. H.; Duwez, P. *Nature* **1960**, *187*, 869–870.
(53) Seto, J. Y. W. *J. Appl. Phys.* **1975**, *46*, 5247–5254.
(54) Lin, V. S.-Y.; Motesharei, K.; Dancil, K.-P. S.; Sailor, M. J.; Ghadiri, M. R. *Science* **1997**, *278*, 840–843.
(55) Pavesi, L.; Dal Negro, L.; Mazzoleni, C.; Franzò, G.; Priolo, F. *Nature* **2000**, *408*, 440–444.
(56) Vlasov, Y. A.; Bo, X. Z.; Sturm, J. C.; Norris, D. J. *Nature* **2001**, *414*, 289–293.
(57) Cui, Y.; Lieber, C. M. *Science* **2001**, *291*, 851–853.
(58) Xiang, J.; Lu, W.; Hu, Y.; Wu, Y.; Yan, H.; Lieber, C. M. *Nature* **2006**, *441*, 489–493.
(59) Tian, B.; Zheng, X.; Kempa, T. J.; Fang, Y.; Yu, N.; Yu, G.; Huang, J.; Lieber, C. M. *Nature* **2007**, *449*, 885–889.
(60) Atwater, H. A.; Polman, A. *Nat. Mater.* **2010**, *9*, 205–213.

(61) Foster, M. A.; Salem, R.; Geraghty, D. F.; Turner-Foster, A. C.; Lipson, M.; Gaeta, A. L. *Nature* **2008**, *456*, 81–84.
(62) Leuthold, J.; Koos, C.; Freude, W. *Nat. Photonics* **2010**, *4*, 535–544.
(63) Reed, G. T.; Mashanovich, G.; Gardes, F. Y.; Thomson, D. J. *Nat. Photonics* **2010**, *4*, 518–526.
(64) Liu, A.; Jones, R.; Liao, L.; Samara-Rubio, D.; Rubin, D.; Cohen, O.; Nicolaescu, R.; Paniccia, M. *Nature* **2004**, *427*, 615–618.
(65) Lin, H.; Weng, W.; Ren, J.; Qiu, L.; Zhang, Z.; Chen, P.; Chen, X.; Deng, J.; Wang, Y.; Peng, H. *Adv. Mater.* **2014**, *26*, 1217–1222.
(66) He, R.; Day, T. D.; Krishnamurthi, M.; Sparks, J. R.; Sazio, P. J. a; Gopalan, V.; Badding, J. V. *Adv. Mater.* **2013**, *25*, 1461–1467.
(67) Martinsen, F. a; Smeltzer, B. K.; Nord, M.; Hawkins, T.; Ballato, J.; Gibson, U. J. *Sci. Rep.* **2014**, *2*, 591.
(68) Won, D.-J.; Ramirez, M. O.; Kang, H.; Gopalan, V.; Baril, N. F.; Calkins, J.; Badding, J. V.; Sazio, P. J. A. *Appl. Phys. Lett.* **2007**, *91*, 161112.
(69) Healy, N.; Mailis, S.; Bulgakova, N. M.; Sazio, P. J. a; Day, T. D.; Sparks, J. R.; Cheng, H. Y.; Badding, J. V; Peacock, A. C. *Nat. Mater.* **2014**, *13*, 1122–1127.
(70) Mehta, P.; Healy, N.; Day, T. D.; Badding, J. V; Peacock, A. C. *Opt. Express* **2012**, *20*, 26110–26116.
(71) Peacock, A. C.; Mehta, P.; Horak, P.; Healy, N. *Opt. Lett.* **2012**, *37*, 3351–3353.
(72) Gumennik, A.; Wei, L.; Lestoquoy, G.; Stolyarov, A. M.; Jia, X.; Rekemeyer, P. H.; Smith, M. J.; Liang, X.; Grena, B. J.-B.; Johnson, S. G.; Gradečak, S.; Abouraddy, A. F.; Joannopoulos, J. D.; Fink, Y. *Nat. Commun.* **2013**, *4*, 2216.
(73) Ballato, J.; Hawkins, T.; Foy, P.; Stolen, R.; Kokuoz, B.; Ellison, M.; McMillen, C.; Reppert, J.; Rao, A. M.; Daw, M.; Sharma, S. R.; Shori, R.; Stafsudd, O.; Rice, R. R.; Powers, D. R. *Opt. Express* **2008**, *16*, 18675–18683.
(74) Sazio, P. J. a.; Amezcua-Correa, A.; Finlayson, C. E.; Hayes, J. R.; Scheidemantel, T. J.; Baril, N. F.; Jackson, B. R.; Won, D.-J.; Zhang, F.; Margine, E. R.; Gopalan, V.; Crespi, V. H.; Badding, J. V. *Science* **2006**, *311*, 1583–1586.
(75) Orf, N. D.; Shapira, O.; Sorin, F.; Danto, S.; Baldo, M. A.; Joannopoulos, J. D.; Fink, Y. *Proc. Natl. Acad. Sci.* **2011**, *108*, 4743–4747.
(76) Morris, S.; Hawkins, T.; Foy, P.; McMillen, C.; Fan, J.; Zhu, L.; Stolen, R.; Rice, R.; Ballato, J. *Opt. Mater. Express* **2011**, *1*, 1141–1149.
(77) Hou, C.; Jia, X.; Wei, L.; Stolyarov, A. M.; Shapira, O.; Joannopoulos, J. D.; Fink, Y. *Nano Lett.* **2013**, *13*, 975–979.
(78) Wang, D.; Shi, Z. *J. Mater. Synth. Process.* **2001**, *9*, 241–246.
(79) Hull, R. *Properties Of Crystalline Silicon*; c2006 ed.; The Institution of Electrical Engineers: London, 2005; Vol. 1.
(80) Finlayson, C. E.; Amezcua-Correa, a.; Sazio, P. J. a.; Baril, N. F.; Badding, J. V. *Appl. Phys. Lett.* **2007**, *90*, 132110.
(81) Lagonigro, L.; Healy, N.; Sparks, J. R.; Baril, N. F.; Sazio, P. J. a.; Badding, J. V.; Peacock, A. C. *Appl. Phys. Lett.* **2010**, *96*, 041105.
(82) Galvagno, G.; Ferla, A. La. *Semicond. Sci. Technol.* **1999**, *1433*.
(83) *Desk Handbook: Phase Diagrams for Binary Alloys*; Okamoto, H., Ed.; ASM International, 2000.
(84) Standage, A. E.; Gani, M. S. *J. Am. Ceram. Soc.* **1967**, *50*, 101–105.
(85) *Aluminum: Properties and Physical Metallurgy*; Hatch, J. E., Ed.; ASM International: Metals Park, Ohio, 1984.

(86) Inatomi, Y.; Onishi, F.; Nagashio, K.; Kuribayashi, K. *Int. J. Thermophys.* **2007**, *28*, 44–59.
(87) Aksay, I. A.; Pask, J. A.; Davis, R. F. *J. Am. Ceram. Soc.* **1979**, *62*, 332–336.
(88) Pfann, W. G. *Science* **1962**, *135*, 1101–1109.
(89) Olson, G. L.; Roth, J. A. *Mater. Sci. Reports* **1988**, *3*, 1–77.
(90) Nordstrand, E. F.; Dibbs, A. N.; Eraker, A. J.; Gibson, U. J. *Opt. Mater. Express* **2013**, *3*, 651–657.
(91) Atkins, P. W.; De Paula, J. *Physical Chemistry*; 9th ed.; W. H. Freeman, 2010.
(92) Monro, T. M.; Ebendorff-Heidepriem, H. *Annu. Rev. Mater. Res.* **2006**, *36*, 467–495.
(93) Sazio, P. J. A.; Amezcua-Correa, A.; Finlayson, C. E.; Hayes, J. R.; Scheidemantel, T. J.; Baril, N. F.; Jackson, B. R.; Won, D.-J.; Zhang, F.; Margine, E. R.; Gopalan, V.; Crespi, V. H.; Badding, J. V. *Science* **2006**, *311*, 1583–1586.
(94) Peacock, A. C.; Sparks, J. R.; Healy, N. *Laser Photon. Rev.* **2014**, *8*, 53–72.
(95) Healy, N.; Mailis, S.; Bulgakova, N. M.; Sazio, P. J. A.; Day, T. D.; Sparks, J. R.; Cheng, H. Y.; Badding, J. V; Peacock, A. C. *Nat. Mater.* **2014**, *13*, 1122–1127.
(96) Tyagi, H. K.; Schmidt, M. A.; Prill Sempere, L.; Russell, P. S. *Opt. Express* **2008**, *16*, 17227.
(97) Chesini, G.; Cordeiro, C. M. B.; de Matos, C. J. S.; Fokine, M.; Carvalho, I. C. S.; Knight, J. C. *Opt. Express* **2009**, *17*, 1660.
(98) Wei, L.; Alkeskjold, T. T.; Bjarklev, A. *Appl. Phys. Lett.* **2010**, *96*, 241104.
(99) Yu, Z.; Margulis, W.; Tarasenko, O.; Knape, H.; Fonjallaz, P.-Y. *Opt. Express* **2007**, *15*, 14948.
(100) Stolyarov, A.; Wei, L.; Shapira, O.; Sorin, F.; Chua, S.; Joannopoulos, J.; Fink, Y. *Nat. Photonics* **2012**, *6*, 229–233.
(101) Yaman, M.; Khudiyev, T.; Ozgur, E.; Kanik, M.; Aktas, O.; Ozgur, E. O.; Deniz, H.; Korkut, E.; Bayindir, M. *Nat. Mater.* **2011**, *10*, 494–501.
(102) Ballato, J.; Hawkins, T.; Foy, P.; Stolen, R.; Kokuoz, B.; Ellison, M.; McMillen, C.; Reppert, J.; Rao, A. M.; Daw, M.; Sharma, S. R.; Shori, R.; Stafsudd, O.; Rice, R. R.; Powers, D. R. *Opt. Express* **2008**, *16*, 18675.
(103) Ballato, J.; Hawkins, T.; Foy, P.; McMillen, C.; Burka, L.; Reppert, J.; Podila, R.; Rao, A. M.; Rice, R. R. *Opt. Express* **2010**, *18*, 4972–4979.
(104) Dragic, P.; Hawkins, T.; Foy, P.; Morris, S.; Ballato, J. *Nat. Photonics* **2012**, *6*, 629–635.
(105) Scott, B. L.; Pickrell, G. *IEEE Photonics Technol. Lett.* **2009**, *21*, 1798–1800.
(106) Tyagi, H. K.; Lee, H. W.; Uebel, P.; Schmidt, M. A.; Joly, N.; Scharrer, M.; Russell, P. S. J. *Opt. Lett.* **2010**, *35*, 2573–2575.
(107) Tuniz, A.; Kuhlmey, B. T.; Lwin, R.; Wang, A.; Anthony, J.; Leonhardt, R.; Fleming, S. C. *Appl. Phys. Lett.* **2010**, *96*, 191101.
(108) Tuniz, A.; Kaltenecker, K. J.; Fischer, B. M.; Walther, M.; Fleming, S. C.; Argyros, A.; Kuhlmey, B. T. *Nat. Commun.* **2013**, *4*, 2706.
(109) Qu, H.; Semenikhin, O.; Skorobogatiy, M. *Smart Mater. Struct.* **2015**, *24*, 025012.
(110) Borisova, Z. U. *Glassy semiconductors.*; New York : Plenum Press, c1981., 1981.
(111) Varshneya, A. K. Fundamentals of inorganic glasses, 1994.
(112) Won, R. *Nat. Photonics* **2011**, *5*, 725–725.
(113) Kaufman, J. J.; Tao, G.; Shabahang, S.; Banaei, E.-H.; Deng, D. S.; Liang, X.; Johnson, S. G.; Fink, Y.; Abouraddy, A. F. *Nature* **2012**, *487*, 463–467.
(114) Gumennik, A.; Wei, L.; Lestoquoy, G.; Stolyarov, A. M.; Jia, X.; Rekemeyer, P. H.; Smith, M. J.; Liang, X.; Grena, B. J.-B.; Johnson, S. G.; Gradečak, S.; Abouraddy, A. F.; Joannopoulos, J. D.; Fink, Y. *Nat. Commun.* **2013**, *4*, 2216.

(115) Aktas, O.; Ozgur, E.; Tobail, O.; Kanik, M.; Huseyinoglu, E.; Bayindir, M. *Adv. Opt. Mater.* **2014**, *2*, 618–625.
(116) Rayleigh, Lord. *Proc. London Math. Soc.* **1879**, *s1-11* , 57–72.
(117) Rayleigh, Lord. *Philos. Mag. Ser. 5* **2010**, *34*, 145–154.
(118) Patnaik, P. *Handbook of Inorganic Chemicals*; McGraw-Hill, 2003.
(119) Nishi, T.; Shibata, H.; Ohta, H. *Mater. Trans.* **2003**, *44*, 2369–2374.
(120) Tomotika, S. *Proc. R. Soc. A Math. Phys. Eng. Sci.* **1935**, *150*, 322–337.
(121) Doremus, R. H. *J. Appl. Phys.* **2002**, *92*, 7619.
(122) Glazov, V. M.; Chizhevskaia, S. N.; Glagoleva, N. N.; Glazov, V. M. *Liquid semiconductors.*; Monographs in semiconductor physics: v. 2; New York, Plenum Press, 1969., 1969.
(123) Sato, Y.; Nishizuka, T.; Tachikawa, T.; Hoshi, M.; Yamamura, T.; Waseda, Y. *HIGH Temp. Press.* **2000**, *32*, 253–260.
(124) Dereniak, E. L.; Boreman, G. D. Infrared detectors and systems, 1996.
(125) Yin, T.; Cohen, R.; Morse, M. M.; Sarid, G.; Chetrit, Y.; Rubin, D.; Paniccia, M. J. *Opt. Express* **2007**, *15*, 13965.
(126) Liu, J.; Beals, M.; Pomerene, A.; Bernardis, S.; Sun, R.; Cheng, J.; Kimerling, L. C.; Michel, J. *Nat. Photonics* **2008**, *2*, 433–437.
(127) Ritter, D.; Zeldov, E.; Weiser, K. *Phys. Rev. B* **1988**, *38*, 8296–8304.
(128) Sorin, F.; Abouraddy, a. F. A. F.; Orf, N.; Shapira, O.; Viens, J.; Arnold, J.; Joannopoulos, J. D. D.; Fink, Y. *Adv. Mater.* **2007**, *19*, 3872–3877.
(129) Dreyer, K. *Am. J. Phys.* **1991**, *59*, 619.
(130) Capasso, F. *Science* **1987**, *235*, 172–176.
(131) Ghahramani, E.; Sipe, J. E. *Phys. Rev. B* **1989**, *40*, 12516–12519.
(132) Park, M. *Science (80-.).* **1997**, *276*, 1401–1404.
(133) Xia, Y.; Whitesides, G. M. *Angew. Chemie Int. Ed.* **1998**, *37*, 550–575.
(134) Whitesides, G. M.; Ostuni, E.; Takayama, S.; Jiang, X.; Ingber, D. E. *Annu. Rev. Biomed. Eng.* **2001**, *3*, 335–373.
(135) Feng, L.; Li, S.; Li, Y.; Li, H.; Zhang, L.; Zhai, J.; Song, Y.; Liu, B.; Jiang, L.; Zhu, D. *Adv. Mater.* **2002**, *14*, 1857–1860.
(136) Nagpal, P.; Lindquist, N. C.; Oh, S.-H.; Norris, D. J. *Science* **2009**, *325*, 594–597.
(137) Geissler, M.; Xia, Y. *Adv. Mater.* **2004**, *16*, 1249–1269.
(138) Qin, D.; Xia, Y.; Whitesides, G. M. *Nat. Protoc.* **2010**, *5*, 491–502.